# CHARGED-CURRENT NEUTRINO INTERACTIONS

*H. Eugene Fisk*

Fermilab, Batavia, Illinois 60510

*Frank Sciulli*

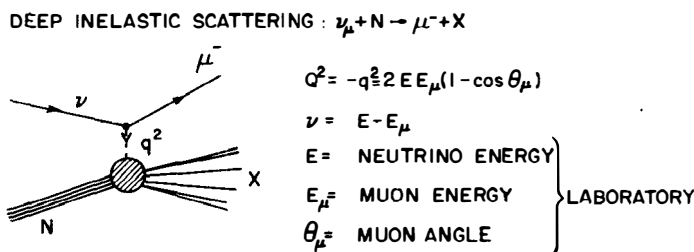Columbia University, New York, New York 10027

CONTENTS

499

# 1. INTRODUCTION

## 1.1 Deep Inelastic Scattering

This article is primarily intended to review the status of the deep inelastic, charged-current scattering of neutrinos from nucleons. Processes of the form, $\nu_\mu + N \rightarrow \mu^- + X$, have been an important subject for research since such processes were found to have the profound simplicity referred to as scaling. This high-energy feature was first seen in lower-energy electron and neutrino scattering experiments (Miller et al 1972, Bodek et al 1973, Eichten et al 1973). In this reaction, the target nucleon, N, is at rest in the laboratory, and the final-state hadron system, X, generally consists of an assemblage of at least one nucleon and several mesons.

The neutrino-nucleon reaction is pictured in Figure 1, where the conventional notation is defined. The principle goal of research is to further our understanding of the structure of the nucleon at the bottom vertex. The most physically intuitive framework to describe that structure is in terms of parton constituents (e.g. Feynman 1969, 1974, Bjorken & Paschos 1969). (The evidence strongly indicates that these partons largely have the properties expected of quarks.) The weak interaction is assumed to be well understood and serves as a tool for investigating the elementary neutrino-quark interaction.

Subsequently, in this introduction, we show how the general features of the scaling hypothesis follow from the assumption of nearly free quarks inhabiting the nucleon, and we derive the relevant formulae from a simple, physical picture. (For a more complete and accurate formulation, see Feynman 1972 or Close 1979). We also briefly review the relevant properties of the neutrino, its charged-current interactions

**DEEP INELASTIC SCATTERING :** $\nu_\mu + N \rightarrow \mu^- + X$



$Q^2 = -q^2 \stackrel{\sim}{=} 2 E E_\mu (1 - \cos\theta_\mu)$

$\nu = E - E_\mu$

$E =$ NEUTRINO ENERGY

$E_\mu =$ MUON ENERGY ⎫ LABORATORY

$\theta_\mu =$ MUON ANGLE ⎭

*Figure 1* Our conception of a neutrino-nucleon reaction, in which the neutrino converts to a $\mu^-$ with the emission of a positive intermediate vector boson. This weak virtual particle interacts with the nucleon to produce a hadronic final state consisting of baryons and mesons (X). At high-momentum transfers (large $Q^2$), the boson wavelength is short enough so that a single constituent of the nucleon interacts.

with other elementary targets, the quark model of nucleon structure, the anticipated form of the inelastic cross section, and the tests and complications of the quark model using deep inelastic data. Readers familiar with the underlying rationale and principles may wish to proceed directly to later sections for a review of the current experimental situation.

## 1.2 The Neutrino: Intrinsic Properties

The neutrino probe is a unique particle in its own right. As a lepton, it does not partake of the strong (nuclear) forces; because it is uncharged, it does not interact electromagnetically. It has half-integer spin, and fits comfortably into a coherent picture of the world of leptons. Because there are three known charged leptons ($e^-$, $\mu^-$, $\tau^-$), neutrinos are thought to also come in three varieties ($\nu_e$, $\nu_\mu$, $\nu_\tau$). Only the first two of these have been directly observed to interact with matter, but it is expected that the $\nu_\tau$ will be similarly observed within a few years. We anticipate that the $\nu_\tau$ will, like the others, preserve throughout its interactions its own "tau-ness" just as the interactions of the electron and muon varieties are observed to conserve electron and muon numbers, respectively.

While all neutrinos have well-known charge and spin, our knowledge and understanding of some other important properties of neutrinos are hazy. Lepton number conservation is one example. The evidence seems strong that each charged lepton and its associated neutrino carry their own lepton number, and that these are individually conserved. Some proposed schemes for lepton number assignment and conservation have been ruled out experimentally (Willis et al 1980). There are other schemes consistent with present experimental data, but there is no compelling evidence for any violation of the usual electron, muon, and tau number assignment and conservation (see review by Primakoff & Rosen 1981).

The value of the neutrino rest mass will always be open to experimental tests. There have been hints of nonzero mass for electron neutrinos (Lubimov et al 1980), but these have yet to be corroborated. We know with confidence that the electron neutrino mass is less than about $60\,eV/c^2$, the muon neutrino mass is less than $600\,keV/c^2$, and the tau neutrino is less massive than $250\,MeV/c^2$ (see review by Sciulli 1980). Current experimental work is being undertaken to reduce these limits, because the finiteness of neutrino mass is a fundamental question in both particle physics and cosmology. However, the mass of muon neutrinos is certainly well below where it could kinematically affect results on charged-current scattering from nucleons.

Another topic of current interest involves both nonzero neutrino mass and the violation of lepton number. If neutrinos were massive and conservation of lepton number were violated, spontaneous transitions might occur between neutrino types. This phenomenon, known as neutrino oscillations, was originally proposed by Pontecorvo (1957). Under appropriate conditions, an initially pure beam of, for example, $\nu_\mu$ would make spontaneous transitions to another neutrino type. The flux of $\nu_\mu$ would therefore depend on both energy and distance from the production point (for a review, see Baltay 1981 or Trilling 1980). While there have been some favorable hints, there is again no compelling evidence that such phenomena occur.

## 1.3    The Charged-Current Interactions

Neutrinos have only been observed to interact with matter through the weak force. There exist both charged- and neutral-current forms of the weak interaction; neutrinos partake of both. We confine ourselves in this article to the charged-current reactions, since these give the most direct information on nucleon structure. Neutral-current reactions are studied primarily to determine the properties of the neutral-current force. (For a review of neutral current structure, see Hung & Sakurai 1981.) The charged-current forces are thought to be well understood at present energies to within a few percent (for review, see Sakurai 1981).

The simplest process exemplifying charged-current interactions is the decay of the muon:

$$\mu^- \rightarrow e^- + \bar{\nu}_e + \nu_\mu. \qquad\qquad 1.$$

In this case, the muon spontaneously disintegrates into a muon type neutrino and an electron with its associated antineutrino. The muon lifetime provides a direct measure of the coupling strength of the weak interactions: the Fermi constant $G = 1.166 \times 10^{-5}\,\mathrm{GeV}^{-2}$. The other observed features of the final-state particles, particularly those of the electron, demostrate that the weak interaction underlying the decay maximally violates parity conservation (i.e. the $V - A$ interaction). In its simplest form, this principle requires that any weakly interacting fermion (including leptons) will interact at high velocity ($v \approx c$) only if the fermion is polarized left-handedly or if the antifermion is polarized right-handedly. In other words, high-velocity right-handed fermions and left-handed antifermions neither interact nor are produced by weak interactions. A direct consequence of this principle is that, in muon decay, the low-mass $\nu_\mu$ is always left-handed. The $\bar{\nu}_e$ is always polarized right-handedly, and the electron prefers left-handed spin orientation unless it has very low energy. This feature is observed.

Our detailed understanding of muon decay permits us to calculate directly the analogous production cross section involving a beam of muon neutrinos incident on a target of electrons:

$$\nu_\mu + e^- \rightarrow \mu^- + \nu_e.$$  2.

This process has been observed and found to comply with expectations (Büsser 1981). For center-of-mass energies ($s^{1/2}$) large compared with the electron or muon mass, the cross section per unit solid angle for the outgoing muon is

$$\frac{d\sigma}{d(\cos\theta)} = \frac{G^2 s}{2\pi},$$  3.

where $\theta$ refers to the angle of the final-state muon with respect to the incident neutrino in the center-of-mass system. The dependence on the square of the center-of-mass energy is a consequence of the point-like structure of the weak interaction at presently available energies. Dimensional considerations require the cross section to depend on energy in this way. For energies at which the finite range of the weak interactions are probed, the formula is still appropriate with the modification $G \rightarrow G/(1 + Q^2/M_W^2)^2$, where $M_W$ is the mass of the intermediate vector boson exchanged in the weak interaction.

The angular dependence of this cross section (Equation 3) is a consequence of the particle angular momenta and the $V - A$ character. In the center-of-mass system, the two colliding leptons only interact if they are spinning opposite to their respective directions of motion, as previously stated. Their spins cancel, so that zero total angular momentum characterizes the collision. The angular distribution in the center of mass is therefore isotropic, as reflected in Equation 3.

We see that our understanding of the structure of charged-current interactions permits direct calculation of cross sections between neutrinos and elementary fields such as the electron. It follows that the cross section of neutrinos interacting with other fields, like quarks, are similarly calculable. We return to these calculations after a brief review of the quark model of hadron structure.

## 1.4  The Quark Model of Nucleon Structure

The idea of elementary spin-$\frac{1}{2}$ fields (quarks), which, in bound states, constitute all hadrons, is now a familiar one. It was originally posited to explain the periodicity in hadron spectroscopy, where it has had renowned success (Gell-Mann 1964, Zweig 1964). The quarks, with fractional charge and baryon number, give hadrons their properties

(spin, charge, strangeness, etc). We were faced, however, with a singular problem: the quarks could not be isolated (at least easily) from hadronic matter. Their spin, charge, and other properties could not be measured in the usual way (e.g. passing isolated quarks through electric and magnetic fields). Such measurements clearly require a different approach. The inelastic scattering of leptons from nucleons provides such a technique.

In the quark model, there are strong spectroscopic reasons for assuming the existence of at least four quark and four antiquark types: u, d, s, c. (The newest quark flavor, b, and its presumed partner, t, are not essential to our discussion.) The s and c quarks carry the quanta of strangeness and charm, respectively. The u and c quarks have electric charge equal to $+\frac{2}{3}$, and d and s carry $-\frac{1}{3}$ of the elementary proton charge. Protons and neutrons, the target nucleons, obtain their quantum numbers from the respective valence combinations (uud) and (udd). In general, additional sea pairs of quark-antiquark, e.g. u$\bar{\text{u}}$, d$\bar{\text{d}}$, etc, could be present. If we picture a nucleon traveling at very high momentum, $P$, this momentum will be constituted by fractions, $\xi_i P$, carried by the constituents. We might intuitively guess that the largest single fraction will be carried by the valence quarks, a smaller fraction carried by the sea quarks, and an unknown amount carried by nucleon constituents that do not interact directly with neutrinos. Experimentally the noninteracting part is about half of the total, and is likely to originate in the fields responsible for the binding of the quarks (e.g. gluons). The sea constituency may consist primarily of the low-mass variety quark since it is expected that a kinematic penalty exists for including more massive quarks in the nucleon wave function.

## 1.5 *Neutrinos Interacting with (Free) Quarks*

The interaction of a neutrino with a free elementary d quark would be similar to the interaction of neutrinos with electrons,

$$\nu_\mu + \text{d} \rightarrow \mu^- + \text{u}, \qquad\qquad 4.$$

and would therefore give the same cross section as Equation 3. Neutrinos could not interact directly with u quarks, since no charge-$\frac{5}{3}$ quark exists for the final state. However, we can have the process

$$\bar{\nu}_\mu + \text{u} \rightarrow \mu^+ + \text{d}. \qquad\qquad 5.$$

This reaction is directly analogous to Reaction 4 with one notable exception: the $\bar{\nu}_\mu$ (right-handed) and u (left-handed) give unit total angular momentum, so that the cross section for antineutrinos scattering

from quarks is that for neutrinos (Equation 3) multiplied by the square of the angular-momentum-one amplitude, $(1 + \cos \theta)/2$.

Table 1 summarizes in the second column the differential center-of-mass cross sections for the scattering of neutrinos (and antineutrinos) from quarks (and antiquarks). Since, for example, the net angular momentum of $\bar{\nu}_\mu \bar{d}$ is the same as that for $\nu_\mu d$, the cross section is identical. For completeness, we add the scattering of neutrinos from hypothetical spin-zero constituents (k partons), which contains the spin-$\frac{1}{2}$ rotation element, $\cos \theta/2$, and an additional factor-of-two increase over the spin-$\frac{1}{2}$ case, where averaging over target spins reduces the cross section. The three forms of the cross section in the second column are complete. Any higher-spin elementary target will scatter with some linear combinations of these. (This follows from the spin-one nature of the weak force).

The target quarks are, of course, not really free. They are bound in hadrons, which complicates the analysis. However, at high energies the center-of-mass scattering angle, $\theta$, is directly related to the inelasticity of the process:

$$y \equiv 1 - E_\mu /E, \qquad\qquad 6.$$

where $E_\mu$ is the outgoing laboratory muon energy and $E$ is the incident neutrino energy. This is demonstrated in Figure 2. This relationship provides a critical interpretative step, so we reiterate: *measurement of laboratory energies only, in an event, permits determination of the center-of-mass scattering angle between the neutrino and the outgoing muon*. Since $1 - y = (1 + \cos \theta)/2$, it follows that the high-energy differential cross sections in y are as given in the third column of Table 1.

The fact that the quarks are moving inside the nucleon, particularly that they have longitudinal momenta, is important to the energy

**Table 1**   Cross sections for neutrino quark scatterings

| Collision | $\dfrac{d\sigma}{d(\cos \theta)}$ | $\dfrac{d\sigma}{dy}$ |
|---|---|---|
| $\nu_\mu d,\ \bar{\nu}_\mu \bar{d}$ | $\dfrac{G^2 s}{2\pi}$ | $\dfrac{G^2 s}{\pi}$ |
| $\bar{\nu}_\mu u,\ \nu_\mu \bar{u}$ | $\dfrac{G^2 s}{2\pi}\left(\dfrac{1 + \cos \theta}{2}\right)^2$ | $\dfrac{G^2 s}{\pi}(1-y)^2$ |
| $\nu_\mu K,\ \bar{\nu}_\mu K$ | $2\dfrac{G^2 s}{2\pi}\cos^2 \dfrac{\theta}{2}$ | $2\dfrac{G^2 s}{\pi}(1-y)$ |
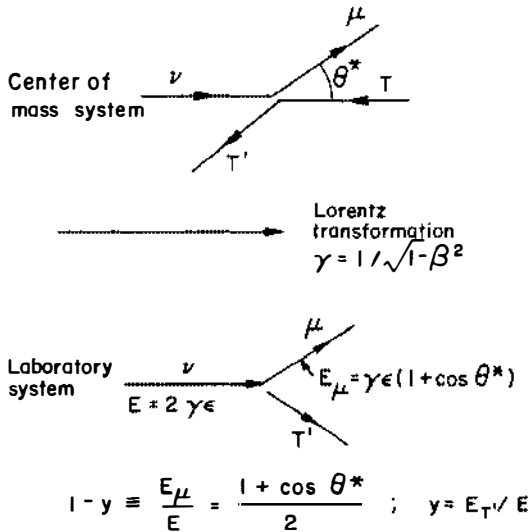
*Figure 2*   The scaling $y$ variable. At high energies where all masses are small compared to particle energies $(\varepsilon)$ in the center-of-momentum frame, the collision between the neutrino and an elementary fermion field, $T$, is essentially elastic. The event scattering angle in this frame $(\theta^*)$ is directly calculable from the event inelasticity $(y)$ of the reaction. The $y$ value is obtained from the measured laboratory neutrino energy and the final-state muon energy. The spins of the nucleon constituents determine the $\theta^*$, or $y$, dependence of the cross section.

dependence of the cross section. Figure 3 shows the neutrino incident on the target quark in the center of momentum of the neutrino-quark system. In this frame, the proton has total momentum $P$, and the quark has a fraction $\xi$ of this. The chosen Lorentz frame then defines the neutrino to have the same momentum as the struck quark, $\xi P$. The cross section is proportional to $s_{\nu q}$: the square of the total four-momentum for the neutrino-quark system. This is just $s_{\nu q} = (2\xi P)^2$. The square of the four-momentum for the entire neutrino-nucleon
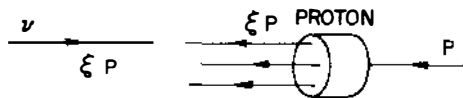


*Figure 3*   The collision between the neutrino and proton constituent as viewed in the Lorentz frame in which the total momentum between them is zero. In this frame, the proton has (high) momentum, $P$, and the constituent has momentum $\xi P$. The square of the center-of-momentum energy between neutrino and constituent is $s_{\nu q} = \xi s$, where $s$ is the square of the invariant energy of the neutrino and nucleon (see text). For laboratory neutrino energy, $E$, and a stationary nucleon target of mass, $M$, then $s \approx 2ME$ at high energies.

system is $s = (\xi P + P)^2 - (\xi P - P)^2 = 4\xi P^2$. Hence $s_{\nu q} = \xi s$. The differential cross section for neutrinos, for example, scattering from d quarks is then a modified version of the entry in Table 1 (Equation 3):

$$\frac{d\sigma}{dy} = \frac{G^2 \xi s}{\pi} \rho(\xi) \, d\xi, \qquad\qquad 7.$$

where $\rho(\xi) \, d\xi$ is the probability for finding such a quark in a frame in which the proton has high momentum with the struck quark fraction between $\xi$ and $\xi + d\xi$.

We still need, for the interpretation of data, a direct empirical measurement of this fractional momentum, $\xi$. One of the most important ideas that has helped us interpret deep inelastic data provides us with an experimental measure of this variable. Refer to Figure 4, where the scattering of the virtual boson from the (nearly massless) quark is shown in the frame in which the (time-like) energy of the boson is zero. By energy conservation, the outgoing massless quark must have energy equal to its incoming energy. The space-like momentum of the propagator must then just equal $\mathbf{q} = 2\xi \mathbf{P}$. It follows that $\xi$ is related to a ratio of Lorentz scalars as

$$\xi = x \equiv \frac{-q^2}{2p \cdot q} = \frac{2EE_\mu(1 - \cos\theta_\mu)}{2M\nu} . \qquad\qquad 8.$$

That is, *the fractional momentum carried by the struck quark may be obtained from measured laboratory quantities*: neutrino energy, $E$; outgoing muon energy, $E_\mu$; with the difference being equal to the laboratory hadron energy, $\nu$; and the outgoing muon angle relative to the incident neutrino direction, $\theta_\mu$. These quantities define the scaling variable, $x$, which approximates the fractional momentum of the struck quark. Of course, this is rigorously correct only in the scaling limit; that is, all energies in the center-of-mass are large compared to all masses, all binding energies, and all internal momenta. This is not and cannot be precisely true. How closely it is approximated is one of the interesting questions to ask of the data.

In a simple scaling model in which a free spin-$\frac{1}{2}$ constituent (q), its antiparticle ($\bar{q}$), and a spin-0 type (k) inhabit the nucleon, the high-energy cross sections for neutrinos incident on a target of equal numbers of neutrons and protons is

$$\frac{d^2\sigma^\nu}{dx \, dy} = \frac{G^2 s}{2\pi} [q^\nu(x) + \bar{q}^\nu(x)(1-y)^2 + 2k(x)(1-y)] \qquad 9a.$$

$$\frac{d^2\sigma^{\bar{\nu}}}{dx \, dy} = \frac{G^2 s}{2\pi} [q^{\bar{\nu}}(x)(1-y)^2 + \bar{q}^{\bar{\nu}}(x) + 2k(x)(1-y)], \qquad 9b.$$

where $q(x)\,dx = x\rho_q(x)\,dx$ for example is the distribution in fractional momentum $x$ multiplied by $x$. The normalization of $q$ is chosen by convention such that it is the total number of quarks per nucleon. Since neutrinos interact, on average, with half the quarks (of appropriate charge), the factor of two appears in the denominator. (The normalization of $k$ becomes model dependent at this stage.)
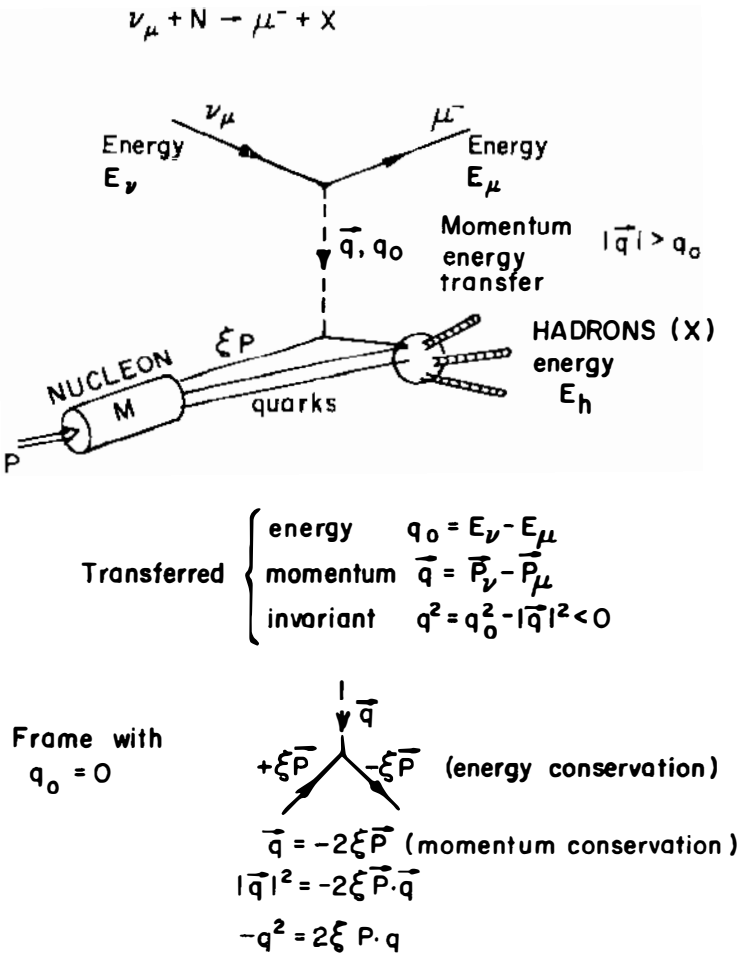


*Figure 4* The scaling variable, $x$. This experimental parameter can be calculated for each event from laboratory energies: $E$ (neutrino), $E_\mu$ (muon), and $\nu$ (hadron); and from muon angle, $\theta_\mu$. The variable $x$ is defined in Equation 8. If all masses, binding energies, and internal momenta can be neglected compared to the longitudinal momenta, $x$ approximates the fraction of nucleon momentum carried by the interacting constituent, $\xi$.

Some important features predicted with these equations are (*a*) The total cross section ($E \gg M$) rises linearly with $s \approx 2ME$, where $M$ is the nucleon mass. (*b*) The momentum distributions of nucleon constituents can be directly extracted, $q(x)$, $\bar{q}(x)$, $k(x)$, and with proper normalization, the integrals of these provide measures of the fractions of momentum carried by the several interacting constituents. The rate of increase of the total cross section with energy is linearly related to these integrals. (*c*) The fraction of antiquark ($\bar{q}$), and of non-spin-$\frac{1}{2}$ k can also be obtained. (*d*) Comparison of these experimental cross sections with analogous data taken with electron or muon beams gives a measure of the charges of the interacting constituents, as discussed below.

It comes as no surprise that the electromagnetic scattering of charged leptons with nucleons, under the same assumptions, has a form very similar to the sum of Equations 9a and 9b. The electromagnetic process is pure V, while Equations 9a and 9b behave like V − A and V + A, respectively. Also, the zero-mass photon propagator gives a $1/Q^2$ dependence, characteristic of Mott scattering. Finally, the strength of the weak interaction is independent of electric charge, while the electromagnetic process is not. Thus, the eN → eX cross section is given by

$$\frac{d^2\sigma^e}{dx\,dy} = \frac{2\pi\alpha^2}{Q^4}\, s\{[r_q^2 q(x) + r_{\bar{q}}^2 \bar{q}(x)][1 + (1-y)^2] + r_k^2 k(x)(1 - y)\}. \quad 10.$$

The parameters $r_q^2$ etc are the mean-square charges of the interacting quark constituents, which measure the relative coupling strengths through the electromagnetic force. Comparison of data from neutrino (weak) scattering with electron or muon (electromagnetic) scattering permits, therefore, measurement of the mean-square charge of interacting constituents.

## 1.6   Quark Types

Table 2 summarizes the quark constituency probed by neutrino beams. The appearance of the Cabibbo angle, $\theta_c$, is a consequence of the weak hadronic current being a linear combination of strangeness-conserving and strangeness-violating parts (Gell-Mann & Levy 1960, Cabibbo 1963). This is observed in the relative leptonic decay rates of kaons and pions, for example.

In Table 2, it is assumed that u, d, s quark masses can be neglected in comparison to center-of-mass energies. At low $Q^2$, this may not be the case for charm (c) production, where $m_c \approx 1.5$ GeV. The parameter $t_c$ is

**Table 2**  Interactions of neutrinos and antineutrinos with various quark types in a four-quark model.[a]

| Reaction | Neutron | Proton | Nucleon |
|---|---|---|---|
| $\nu + d \rightarrow \mu^- + u$ | $d_n \cos^2 \theta_c$ | $d_p \cos^2 \theta_c$ | $(d+u) \cos^2 \theta_c$ |
| $\rightarrow \mu^- + c$ | $d_n \sin^2 \theta_c$ | $d_p \sin^2 \theta_c$ | $(d+u)t_c \sin^2 \theta_c$ |
| $\nu + s \rightarrow \mu^- + c$ | $s_n \cos^2 \theta_c$ | $s_p \cos^2 \theta_c$ | $2s\, t_c \cos^2 \theta_c$ |
| $\rightarrow \mu^- + u$ | $s_n \sin^2 \theta_c$ | $s_p \sin^2 \theta_c$ | $2s \sin^2 \theta_c$ |
| $\nu + \bar{u} \rightarrow \mu^- + \bar{d}$ | $\bar{u}_n \cos^2 \theta_c$ | $\bar{u}_p \cos^2 \theta_c$ | $(\bar{d}+\bar{u}) \cos^2 \theta_c$ |
| $\rightarrow \mu^- + \bar{s}$ | $\bar{u}_n \sin^2 \theta_c$ | $\bar{u}_p \sin^2 \theta_c$ | $(\bar{d}+\bar{u}) \sin^2 \theta_c$ |
| $\nu + \bar{c} \rightarrow \mu^- + \bar{s}$ | $\bar{c}_n \cos^2 \theta_c$ | $\bar{c}_p \cos^2 \theta_c$ | $2\bar{c} \cos^2 \theta_c$ |
| $\rightarrow \mu^- + \bar{d}$ | $\bar{c}_n \sin^2 \theta_c$ | $\bar{c}_p \sin^2 \theta_c$ | $2\bar{c} \sin^2 \theta_c$ |
| $\bar{\nu} + u \rightarrow \mu^+ + d$ | $u_n \cos^2 \theta_c$ | $u_p \cos^2 \theta_c$ | $(d+u) \cos^2 \theta_c$ |
| $\rightarrow \mu^+ + s$ | $u_n \sin^2 \theta_c$ | $u_p \sin^2 \theta_c$ | $(d+u) \sin^2 \theta_c$ |
| $\bar{\nu} + c \rightarrow \mu^+ + s$ | $c_n \cos^2 \theta_c$ | $c_p \cos^2 \theta_c$ | $2c \cos^2 \theta_c$ |
| $\rightarrow \mu^+ + d$ | $c_n \sin^2 \theta_c$ | $c_n \sin^2 \theta_c$ | $2c \sin^2 \theta_c$ |
| $\bar{\nu} + \bar{d} \rightarrow \mu^+ + \bar{u}$ | $\bar{d}_n \cos^2 \theta_c$ | $\bar{d}_p \cos^2 \theta_c$ | $(\bar{d}+\bar{u}) \cos^2 \theta_c$ |
| $\rightarrow \mu^+ + \bar{c}$ | $\bar{d}_n \sin^2 \theta_c$ | $\bar{d}_p \sin^2 \theta_c$ | $(\bar{d}+\bar{u})t_c \sin^2 \theta_c$ |
| $\bar{\nu} + \bar{s} \rightarrow \mu^+ + \bar{c}$ | $\bar{s}_n \cos^2 \theta_c$ | $\bar{s}_p \cos^2 \theta_c$ | $2\bar{s}\, t_c \cos^2 \theta_c$ |
| $\rightarrow \mu^+ + \bar{u}$ | $\bar{s}_n \sin^2 \theta_c$ | $\bar{s}_p \sin^2 \theta_c$ | $2\bar{s} \sin^2 \theta_c$ |

[a] $\theta_c$ = cabibbo angle; $t_c$ = threshold factor for charm quark production. We assume (a) isospin symmetry (e.g. $d_n = u_p$, etc) and (b) charm and strange quark (antiquark) constituency are independent of neutron-proton isospin (e.g. $s_n = s_p$).

included for this case, where the slow rescaling hypothesis is the most natural way to handle the threshold behavior (see Section 4). For $m_c^2 \ll W^2$, where $W$ is the invariant mass of the final-state hadron system, $t_c \rightarrow 1$. We consider this case below.

The net quark and antiquark distributions are defined as: ($x$ dependence assumed)

$$q = u + d + s + c, \tag{10a}$$
$$\bar{q} = \bar{u} + \bar{d} + \bar{s} + \bar{c},$$

where, for example, $u = u(x)$ is the momentum fraction times the probability for finding a u quark with momentum fraction between $x$ and $x + dx$ in the proton. If isospin symmetry is assumed, then the coefficients in Equations 9a and 9b at high energies are

$$q^\nu = q - c + s, \tag{11a}$$
$$\bar{q}^\nu = \bar{q} + \bar{c} - \bar{s}, \tag{11b}$$
$$q^{\bar{\nu}} = q + c - s, \tag{11c}$$
$$\bar{q}^\nu = \bar{q} - \bar{c} + \bar{s}. \tag{11d}$$

We expect, therefore, a slight asymmetry in these coefficients unless the charm content in the nucleon were equal to the strange content. It is expected that the strange content will dominate at present energies, because the strange-quark mass is small in comparison to that of the charm quark.

A measurement of the strange content of the nucleon is obtained from events with two muons in the final state. Such events result from reactions that produce a charm quark, followed by leptonic decay of the charmed particle (e.g. $D^0 \rightarrow K^- \mu^+ \nu_\mu$). Because of the weak selection rules operative in these decays, such events should always have the oppositely charged leptons in the final state, with one from the neutrino collision and the other from the charm decay. Indeed, it is found that the opposite-sign dilepton event rates are at least an order-of-magnitude more intense than same-sign dilepton events. This gives strong evidence that charm production is the dominant mechanism for dilepton production. From Table 2, the contributions to these data in Equations 9a and 9b will be

$$q_{2\mu}^\nu = T[(d + u) \sin^2 \theta_c + 2s \cos^2 \theta_c],$$

$$\bar{q}_{2\mu}^\nu = 0,$$

$$q_{2\mu}^{\bar{\nu}} = 0,$$

$$\bar{q}_{2\mu}^{\bar{\nu}} = T[(\bar{d} + \bar{u}) \sin^2 \theta_c + 2\bar{s} \cos^2 \theta_c]. \qquad 12.$$

Note that neutrinos produce charm from valence quarks, while antineutrinos do not. Here, $T$ includes the threshold dependence for charm production, as well as the total probability for the charmed final state to produce an observable decay lepton. This is discussed at greater length in Section 4.

Events with two leptons of the same electric charge should not occur in the usual four-quark model, since the weak selection rules forbid them. But such events are observed about once in each 2000 charged-current events. Several sources have been hypothesized: (a) $D^0 - \bar{D}^0$ mixing, (b) b-quark constituency of the nucleon, etc. None has provided a universally acceptable explanation.

## 1.7 General Formulation of Deep Inelastic Scattering

Table 3 summarizes the formulae and notation commonly used in the analysis of deep inelastic scattering data. These are valid to first order in the target nucleon mass and ignore the charged-lepton mass relative to the incident neutrino energy. The small asymmetries already discussed

**Table 3** Formulae and notation of deep inelastic scattering

| | |
|---|---|
| $x$ | $E$ = beam (neutrino) energy |
| $y \equiv \nu/E$ | $E_\mu$ = outgoing lepton (muon) energy |
| | $\nu$ = $E - E_\mu$ |
| | $Q^2$ |
| | $s$ = $M^2 + 2ME$ |

Scaling two-quark model
$$\begin{cases} F_2(x, Q^2) \\ 2xF_1(x, Q^2) \\ xF_3(x, Q^2 \end{cases} \qquad \frac{k(x)}{q\,x + q\,x}$$

Neutrino:
$$q(x) \equiv u(x) + d(x) + s(x) + c(x)$$
$$\bar{q}(x) = \bar{u}(x) + \bar{d}(x) + \bar{s}(x) + \bar{c}(x)$$

Muon-electron
$$q^{em}(x) = \tfrac{4}{9}u(x) + \tfrac{1}{9}d(x) + \tfrac{1}{9}s(x) + \tfrac{4}{9}c(x)$$
$$\bar{q}^{em}(x) = \tfrac{4}{9}\bar{u}(x) + \tfrac{1}{9}\bar{d}(x) + \tfrac{1}{9}\bar{s}(x) + \tfrac{4}{9}\bar{c}(x)$$

Neutrino
$$\frac{d^2(\sigma^\nu + \sigma^{\bar\nu})}{dx\,dy} = \frac{G^2 s}{\pi} \left\{ \left(1 - y - \frac{Mxy}{2E}\right) F_2^{wk}(x, Q^2 \right.$$

$$\frac{d^2(\sigma^\nu - \sigma^{\bar\nu})}{dx\,dy} = \frac{G^2 s}{\pi} [y(1 - \tfrac{1}{2}y)xF_3^{wk}$$

Muon-electron
$$\frac{d^2\sigma}{dx\,dy} \quad \frac{4\pi\alpha^2}{Q^4} s \left\{ \left(1 - y - \frac{Mx}{2E}\right.\right.$$

$$\frac{2xF_1}{F_2} \equiv \left(1 + \frac{4M^2x^2}{Q^2}\right) \Big/ (1 + R); \; 0 \le R \le \infty$$

due to the presence of s quarks (with few c quarks) are typically explicitly corrected to provide $F_2$, $R$, and $xF_3$ as defined in the table. Included for completeness are the analogous formulae for the inelastic scattering of muons or electrons.

From this table, we see the following predictions of the simple quark model.

1. Approximate scaling: $F_i(x, Q^2) \approx F_i(x)$. This requires that the total cross section be linearly dependent on energy.
2. Spin-$\tfrac{1}{2}$ dominance (Callan-Gross relation): $R^{wk} \approx R^{em} \approx 0$ (Callan & Gross 1969, Bjorken & Paschos 1969).
3. Quark charges: $F_2^{em}/F_2^{wk} \approx \tfrac{5}{18}$. More precisely, we expect, for negligible charm content,

$$\frac{F_2^{em}}{F_2^{wk}} = \frac{5}{18} \left[ 1 - \frac{3}{5} \frac{s + \bar{s}}{q + \bar{q}} \right]. \qquad 13.$$

4. Number of valence quarks (Gross–Llewellyn Smith sum rule). Table 2 gives the difference of neutrino-antineutrino scattering, well above charm threshold, as

$$\frac{d^2(\sigma^\nu - \sigma^{\bar\nu})}{dx\,dy} = \frac{G^2 s}{\pi}\{[q(x) - \bar q(x)][(1 - (1 - y)^2]$$

$$+ \{[s(x) - \bar s(x)] + [c(x) - \bar c(x)]\}[1 + (1 - y)^2]\}. \qquad 14.$$

We anticipate that $s(x) = \bar s(x)$ and $c(x) = \bar c(x)$. These equalities are expected but are not required by any general principle. In any case, we must have $\int[s(x)/x]dx = \int[\bar s(x)/x]dx$, etc, since the net strangeness (charm) of the nucleon is zero. It follows that

$$\int_0^1 \frac{xF_3(x)}{x}\,dx = \int_0^1 \frac{[q(x) - \bar q(x)]}{x}\,dx = 3, \qquad 15.$$

which is the net number of valence quarks in the nucleon. This is referred to as the Gross–Llewellyn Smith (GLS) sum rule (Gross & Llewellyn Smith 1969).

5. Up-down quark difference (Adler sum rule). From Table 2, we see that the difference between scattering from neutrons and protons is, assuming the strange and charm components cancel,

$$\frac{d^2(\sigma^{\nu n} - \sigma^{\nu p})}{dx\,dy} = \frac{G^2 s}{\pi}[(u - d) - (\bar u - \bar d)(1 - y)^2] \qquad 16.$$

and precisely the reverse $y$ dependence for antineutrinos. This gives rise to the prediction (Adler 1966)

$$\int \frac{xF_1^{\nu n} - xF_1^{\nu p}}{x}\,dx = 1. \qquad 17.$$

This reflects the asymmetry of (uud) and (udd) in protons and neutrons, respectively. To test the Adler sum rule requires the use of hydrogen targets.

## 1.8 Deviations from the Naive Quark Model

From the beginning of work on deep inelastic scattering, it was recognized that scaling should be an approximate phenomenon. Indeed, as it was understood in terms of point-like constituent scattering, it was

simultaneously recognized that nonscaling effects should exist at lower energies. The quarks are not, as assumed in the parton model, precisely free with no transverse momentum since they are bound inside hadrons. It is expected that binding and transverse momentum will produce effects that behave approximately as a power of $1/Q^2$.

For example, the Callan-Gross relation must obtain some violation from such effects. If the spin-$\frac{1}{2}$ constituents have a nonzero transverse momentum, $p_T$, then the collision between quarks is noncolinear at this level, and from this effect alone,

$$R \simeq 4 \; \frac{\langle p_T^2 \rangle}{Q^2}. \hspace{3cm} 18.$$

Similar deviations, in magnitude and in dependence on $Q^2$, are expected from finite quark mass and binding energies.

The other structure functions should also have some $Q^2$ dependence from such effects. The very definition of the variable $x$ and its interpretation as fractional momentum requires the assumption of high $Q^2$. Early interpretations of ep scattering data invoked novel definitions of scaling variables, e.g. $x' = Q^2/(2M\nu + M^2)$, that satisfy the only necessary requirement: $x' \to x$ as $Q^2 \to \infty$. With such definitions, the effect on structure functions could be very big, especially at larger $x$ values, e.g. $F_2(x, Q^2) \simeq F_2(x)[1 + nM^2 x/Q^2(1 - x)]$, if $F_2(x') \simeq (1 - x')^n$ at large $x'$.

Scale-breaking effects could also come from leptons scattering from bound two-quark systems. These subsystems would give scale breaking similar to that discussed above, and could induce finite $R$ values, particularly at large $x$ (Schmidt & Blankenbecler 1977).

## 1.9   Quantum Chromodynamics

There has been considerable enthusiasm in recent years for the theory of quantum chromodynamics (QCD) as a viable theory of strong interactions. This theory describes the strong force binding quarks in hadrons as carried by colored gluons, in a manner similar to the way the photon carries the electromagnetic force in atoms (for review, see Appelquist et al 1978). This theory predicts a pattern of scale breaking in deep inelastic scattering that is different at high $Q^2$ than that anticipated above from bound-state complications. The pattern is dominated by the quark-gluon coupling constant, which, to first order, is $\alpha_s(Q^2) = 12\pi/(33 - 2N_f) \ln(Q^2/\Lambda^2)$. Here $N_f$ is the number of quark flavors, and $\Lambda$ is a scale thus far undefined by the theory, but it is anticipated to lie in the range of strong interaction binding scales, which

is $\sim 10^{-13}$ cm $(0.1 < \Lambda < 0.7$ GeV$)$. (For a recent review of evidence for QCD, see Söding & Wolf 1981.)

The pattern of such perturbative effects is logarithmic in $Q^2$, rather than being a power law. The greatest experimental difficulty lies in comparing structure function data with predictions that have an unknown part falling like a power of $1/Q^2$ and predictions that have a logarithmic dependence.

The prediction for $R$, in perturbative QCD, is particularly simple and direct. It is (Altarelli & Martinelli 1978)

$$2xF_1R(x,\ Q^2) = \frac{\alpha_s(Q^2)}{2\pi}\, x^2 \left[ \int_x^1 \frac{dz}{z^3}\frac{8}{3}\, F_2(z,\ Q^2)\ dz \right.$$

$$\left. + \int_x^1 \frac{dz}{z^3}\, 16\left(1 - \frac{x}{z}\right)\, G(z,\ Q^2)\ dz \right]. \qquad 19.$$

The first term in the brackets comes from perturbative processes in which the constituent quark creates a bremsstrahlung gluon before collision with the neutrino; the second term comes from pair production of quarks by a gluon, hence the dependence on the gluon distribution, $G(x,\ Q^2)$, with subsequent interaction between a quark and the neutrino. The features predicted by this formula are rather striking, as illustrated in Figure 5. There should be a sharp falloff in $x$ at fixed $Q^2$ and a slow (logarithmic) dependence on $Q^2$. Unfortunately the $R$
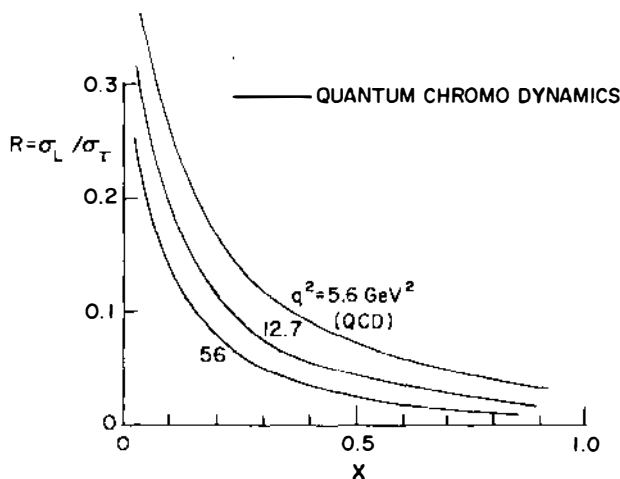


*Figure 5* Predictions for $R$ from quantum chromodynamics (Equation 19). Other contributions can come from mechanisms that produce power law dependence on $1/Q^2$.

parameter is very difficult to measure. We review the available data in
Section 3.

## 2   HIGH-ENERGY NEUTRINO EXPERIMENTS

### 2.1   *Neutrino Beams*

2.1.1   INTRODUCTION   The advent of high-energy accelerators plus the
expected linear energy increase in the cross section gave promise for
extensive studies of neutrino interactions (Pontecorvo 1951, Schwartz
1960). Such studies have come to pass with a variety of different
neutrino beams. Generally, all of these beams are created in long
evacuated pipes as the products of $\pi$- and K-mesons decaying into their
major decay mode: $\mu^- + \nu_\mu$. The parent $\pi$ and K mesons are them-
selves produced by machine energy protons striking a target upstream of
the decay pipe. Downstream of the decay region, there must be
sufficient shielding to remove the high-energy muons. (The muon
intensity accompanying a useful neutrino beam is too intense to allow its
passage through the neutrino detector.)

The earliest accelerator neutrino experiment used neutrinos from a
"bare target" system without any focusing of the meson parents (Danby
et al 1962). Nowadays, the secondary mesons are usually focused to
obtain more neutrino flux. The focusing has been accomplished with
both horn systems and quadrupole magnets. The mesons can also be
momentum selected before they enter the decay region. A momentum-
selected meson beam creates a narrow-band neutrino beam; without
such selection, the neutrino beam is called wide band. The remainder of
this section deals with examples of existing beams.

An example of the present narrow-band neutrino beam layout at
Fermilab is shown in Figure 6. The simultaneous use by several large
and varied detectors, shown here, also exists at CERN. Moreover,
different kinds of beams can be utilized by making relatively minor
changes in the targeting region. One significant difference between the
CERN and Fermilab facilities is that the distance from the midpoint of
the decay region to the detectors is shorter at CERN (600 m). The
Fermilab layout was optimized for 1000 GeV during its initial construc-
tion.

Generally speaking, the bubble chamber experiments with fiducial
tonnage of 1 to 10 tons have opted for wide-band beams that maximize
neutrino flux by focusing the wide-angle, lower-momentum secondaries
in the forward direction. On the other hand, the massive electronic
detectors (300 to 1500 tons) have typically requested beams that accen-

tuate high-energy neutrinos, such as narrow-band beams or quadrupole-focused beams.

Since at high energies the laboratory decay angle, $\theta$, of the high-energy neutrinos intercepting the downstream neutrino detector is small, typically less than a few milliradians, the neutrino energy from a pencil beam of hadron secondaries is accurately given by the approximation

$$E_\nu = E_\nu(\text{max})/(1 + \gamma^2\theta^2), \qquad\qquad 20.$$

where $\gamma$ is the usual ratio of beam hadron energy to rest mass, and $E_\nu(\text{max})$ is the maximum energy neutrino, given in terms of the hadron beam energy by $E_\nu(\text{max}) = E_{\pi,K}[1 - (m_\mu/m_{\pi,K})^2]$. Thus a secondary hadron beam of fixed momentum leads to two distinct energies for zero-degree neutrinos. Which of these energies occurs depends on whether the parent hadron was a K or $\pi$ meson: $E_\nu^\pi(\text{max}) = 0.42\ E_\pi$ and $E_\nu^K(\text{max}) = 0.95\ E_K$.

2.1.2  NARROW-BAND BEAMS  The recognition of the dichromatic nature of the neutrino's energy spectrum led to proposals for accelerator neutrino beams where the correlation between the neutrino's angle and energy could be exploited to determine the energy of each neutrino interaction in a downstream detector (Peterson 1964, Sciulli et al 1970). A by-product of such a beam is the relative ease of measuring and
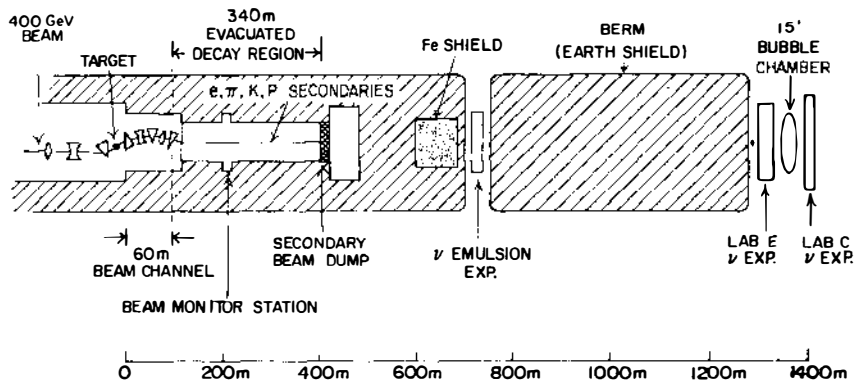


'Figure 6  The Fermilab Neutrino Area in 1980. The several detectors may make simultaneous use of the neutrino beam. During narrow-band beam operation, illustrated here, the extracted proton beam is separated from the momentum-selected secondary beam and dumped prior to the decay pipe. This permits monitoring and measurement of the meson secondaries in the decay pipe for purposes of flux normalization. The transverse dimension has been expanded in the figure for clarity.

monitoring flux (see Figure 6). The first example of such a beam had a maximum energy of 230 GeV. It was brought into operation at Fermilab in 1972–1973 (Limon et al 1974). The optics of this beam consisted of point-to-parallel focusing plus momentum selection ($\Delta p/p \simeq \pm 18\%$). At the CERN SPS a more sophisticated dichromatic beam has operated since 1976 with a momentum bite $\Delta p/p$ of $\pm 5\%$ and a maximum energy of 300 GeV. The CERN beam optics (May et al 1977) is point-to-intermediate focus, followed by additional focusing to parallel. A second-generation Fermilab beam, capable of focusing 350-Ge secondaries, was designed (Edwards & Sciulli 1976) and brought into operation in 1978. It has been used in several recent experiments. Figure 7 shows the correlation implied by Equation 20 between the neutrino interaction radius and neutrino energy for data at ten different beam settings from the Columbia/Caltech-Fermilab-Rochester-Rockefeller (CFRR) experiment located in Lab E. The contributions of neutrinos from $\pi$ and K decay are clearly visible as separate bands.

Momentum bite is only one of the factors determining the average neutrino energy and its spread, $\sigma_E$, at a given detector radius. Other factors affecting energy resolution are the secondary beam angular divergence and parallax, i.e. the fact that neutrinos of different energy originating at different points in the decay pipe reach the detector at a common radius. From Equation 20 the characteristic decay angle, $\theta_o$, is $\gamma^{-1}$. For secondary pions, where $\theta_o$ is less than 1 mrad at high energy, a typical beam angular divergence of $\pm 0.2$ mrad has a substantial effect on the mean neutrino energy and resolution. For neutrinos generated from K mesons, angular divergence does not significantly affect energy resolution. Parallax is important in this case, especially at CERN where the detectors are close to the midpoint of the decay pipe. Although the meson beam momentum bite at CERN is smaller than that at Fermilab, the average energy resolutions are very similar, primarily because of the parallax difference. For the Fermilab beam, tuned to 200 GeV, the $\nu_K(\nu_\pi)$ energy resolution, $\sigma_E/E$, varies from 10 (15)% at the center of the detector to 9 (20)% at the edge of the fiducial volume where the radius is 1.25 (0.75) m.

From measurements of the secondary beam intensity, momentum bite, angular divergence, and $\pi$, K, p beam composition, the absolute neutrino flux can be calculated. As an example, the flux from the Fermilab beam is shown in Figure 8. In addition to the dichromatic components, there is additional calculable flux at the level of 5 (7)% of the $\nu_K$ flux from $K_{\mu_3}(K_{e_3})$ decays as indicated in Figure 8. The $K_{\mu_3}$ flux is more of a nuisance for charged-current studies since it produces
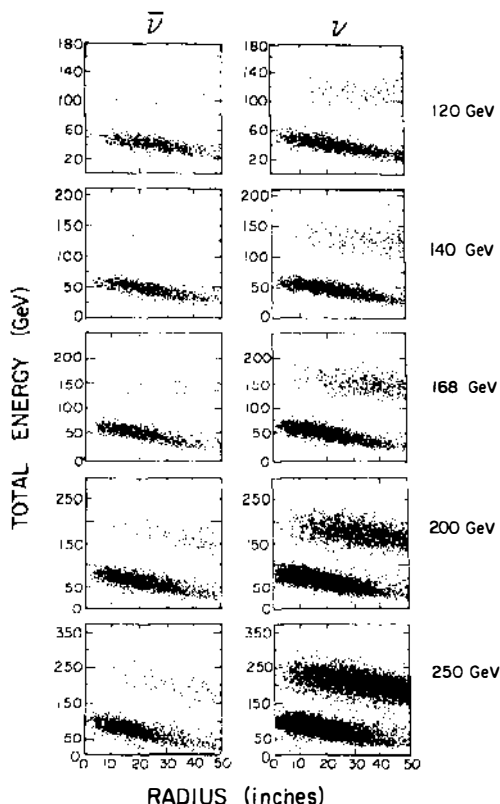
*Figure 7*   Measured correlation in the narrow-band beam between detected neutrino event energies and the radial position of interaction at the Lab E detector (CFRR group). The settings of the beam central momentum for the selected mesons is shown to the right. Negative and positive charged-meson selection produces $\bar{\nu}$ and $\nu$, respectively. The bands correspond to K decay (*upper band*) and $\pi$ decay (*lower band*), respectively. The smaller number of $K^-$ mesons relative to $K^+$ mesons is evident from the comparative paucity of high-energy antineutrino events.

acceptable charged-current data. Unwanted broad-band $\nu_\mu$ and $\bar{\nu}_\mu$ flux is also generated from decays of mesons before momentum selection. Both the CERN and Fermilab beams minimize these neutrinos by targeting the primary proton beam at a large angle (11 to 14 mrad) relative to the neutrino detector direction. The contribution of this wide-band background to a given neutrino data sample is measured by obtaining neutrino data with the beam entrance to the decay pipe blocked. Since this wide-band flux is dominated by decays of low-momentum mesons, it is most important for pion neutrino data where,
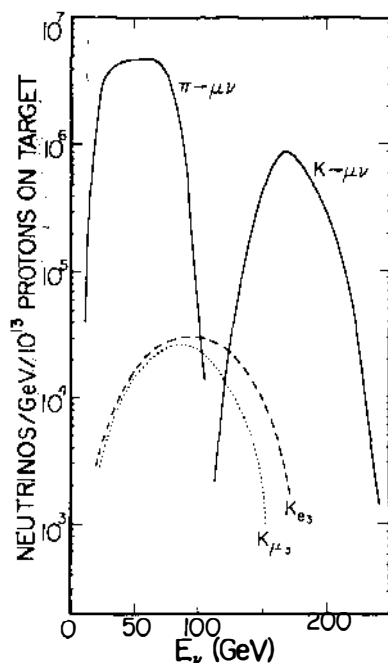
*Figure 8*   The flux of neutrinos at the Fermilab Lab E detector (radius 1.5 m) with the central hadron momentum selected at 200 GeV with positive electric charge. The dichromatic nature of the beam is clear; the small calculable neutrino contaminations from three-body kaon decays are also shown. Background from low-momentum decays before momentum selection of the meson beam produces additional background primarily below 20 GeV. This can be directly measured by stopping the dichromatic beam before its entry into the decay region.

with a secondary momentum of 200 GeV/$c$, it averages 5% and is a maximum of 10% at the lowest energies in the Fermilab beam.

2.1.3   WIDE-BAND BEAMS   Charged-current event rates for the 1000-ton detectors with narrow-band beams are typically a few per machine cycle. For smaller-mass targets, like bubble chambers, and for study of rare processes in massive detectors, it was suggested quite early that beams would be needed where wide-angle, low-momentum secondaries would be focused in the forward direction (van der Meer et al 1963, Giesch et al 1963). It has been possible to build these wide-band beams where almost half of the secondary mesons of a given sign are focused into the decay pipe. Focusing is achieved by pulsing high-current (water-cooled) aluminum horn-shaped conductors to create an azimuthal magnetic field. In these "horn" beams, wide-angle (lower-

energy) secondaries of one sign are focused while those of opposite sign are defocused.

The quadrupole triplet beam, as the name implies, uses quadrupole focusing to produce a beam that eliminates much of the very-low-energy neutrino flux and relatively enhances the high-energy flux from K decays. Because of the nature of quadrupole focusing, sign selection is relatively poor. This beam, at Fermilab, has been especially useful for investigating charm production by neutrinos.

Figure 9 shows the neutrino flux from three different wide-band beams at Fermilab: horn (Grimson & Mori 1978), quadrupole triplet (Skuja et al 1976), and bare target (Stefanski & White 1976). For comparison, the flux that would be generated by a perfectly focused beam, an ideal situation in which all produced mesons are directed toward the neutrino target, is also shown. In all $\nu$ ($\bar{\nu}$) wide-band beams, there is a significant amount of $\bar{\nu}$ ($\nu$) background flux from the secondaries being defocused. When the horn beam focuses negative secondaries to generate antineutrinos, the neutrino flux at energies above 60–80 GeV exceeds the antineutrino flux because of the preponderance of $K^+$ to $K^-$ secondaries. This has motivated the use of
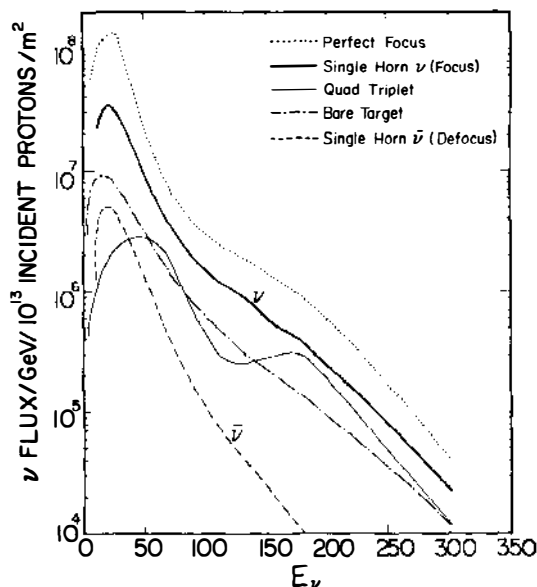


*Figure 9* The calculated flux of neutrinos from various broad-band focusing devices used at Fermilab compared to that which would result from a perfect focusing device. The proton beam energy has been taken to be 400 GeV.

plugs in the central region of the secondary beam to increase the $\bar{\nu}/\nu$ flux ratio at high energies.

A schematic physical layout for the Fermilab horn is shown in Figure 10. The horn is powered with a 100-kA half-sine-wave pulse generated from a 2400-$\mu$F capacitor bank charged to 6 kV. At both CERN and Fermilab, the current pulse has been lengthened from 40 $\mu$s to 1 ms by using a transformer with the capacitor bank on the primary winding and the horn on the secondary winding. This more closely matches the beam extraction period during neutrino operation.

## 2.2  Beam Flux Measurements

2.2.1  MONITORING  Measuring neutrino total cross sections requires knowledge of the absolute neutrino flux and energy spectrum at a given detector radius. This flux can be reliably calculated only for narrow-band beams where the properties of the secondary beam or of the decay muons, which correlate directly with the $\nu_\mu$ flux, can be measured. Required are measurements of the absolute numbers of $\pi$ and K mesons, mean secondary momentum $\langle p \rangle$, momentum spread $\sigma_p$, and beam angular divergence.

Two basic and complementary techniques have been developed to monitor the beam. The method used primarily at Fermilab has been to measure the absolute hadron flux in the decay pipe and the fractions of e, $\mu$, $\pi$, K, and p ($\bar{p}$). The CERN technique also involves measurement of particle fractions, using a similar method. The absolute intensity measurement initially depended heavily on a beam current transformer in the secondary beam but has more recently relied on measuring the absolute number and profile of muons from $\pi$ decay, which along with the K/$\pi$ particle ratio gives the absolute neutrino flux. No method is completely straightforward since the typical narrow-band beam secon-
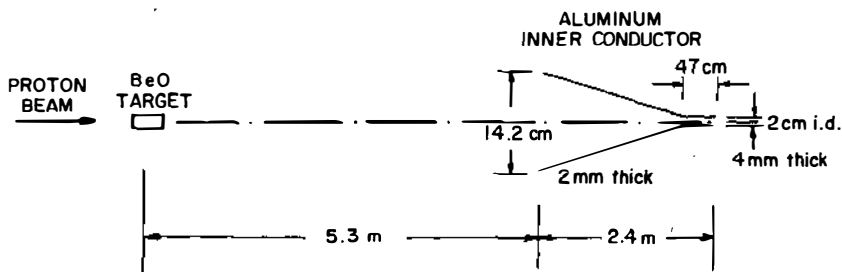


*Figure 10*  The horn at Fermilab, showing the placement relative to the target position and the location of the cylindrical inner conductor. Particles of one sign that penetrate this conductor are focused; those with electric charge of opposite sign are defocussed.

dary flux is $10^9$ to $10^{11}$ particles during a 1-ms spill, i.e. $\sim 10^{13}$ s$^{-1}$ instantaneous rate. This clearly precludes measuring the total number and kinds of beam particles with standard counting techniques.

2.2.2  PARTICLE RATIOS  Both CERN and Fermilab use short (2 m long) focusing Čerenkov detectors with He gas as the radiator to measure the relative numbers of $\pi$'s, K's, and protons in the decay pipe. Unlike typical Čerenkov detectors in particle physics, which tag individual particles, these counters integrate all light traversing a small iris at the focal point during the beam spill. Their length implies that a phototube typically observes $\sim 0.01$ photoelectrons per beam particle. Such short length also means that diffraction effects become important in understanding resolutions. A Čerenkov curve is obtained by recording the light output normalized to beam intensity as a function of Čerenkov pressure, $P$.

At Fermilab, Čerenkov light with angles between 0.7 and 1.0 mrad is transmitted to a photomultiplier tube. Because of the high beam intensity, only a few stages of phototube amplification are needed to provide adequate current. A sample Čerenkov curve, after background subtraction, is shown in Figure 11. The relative fractions of $\pi$, K, and p are proportional to the areas under the peaks. The K/$\pi$ ratios obtained in the CFRR experiment are shown in Figure 12. Measurements at CERN made in similar fashion (de Groot et al 1979), as well as those made using more traditional techniques (Atherton et al 1980), are in good agreement with the CFRR data (Rapidis et al 1981).

These Čerenkov curves contain a wealth of information in addition to particle fractions. A good approximation governing Čerenkov light in



CFRR ČERENKOV COUNTER
+200 GeV
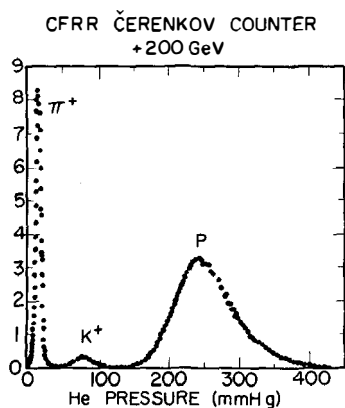
He PRESSURE (mmHg)

Figure 11  The net Čerenkov light per beam particle transmitted through a small (0.7–1 mrad) iris as a function of helium pressure. The peaks occur at the pressures expected for pions, kaons, and protons at this setting of the dichromatic beam (200 GeV). The areas under the peaks are directly proportional to the relative fractions of these particles in the beam.
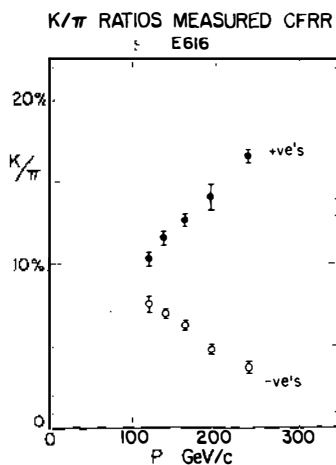
K/$\pi$ RATIOS MEASURED CFRR
E616



*Figure 12*   The ratio of kaons to pions in the Fermi-lab dichromatic beam as a function of beam setting.

this regime is the relation, $\theta_c^2 = 2(n_0 - 1)P/P_0 - (m/p)^2$, between Čerenkov angle ($\theta_c$), pressure (P), index of refraction ($n_0$) calibrated at known pressure ($P_0$), mass (m), and momentum (p). The pressure means of the Čerenkov peaks on the curve are directly related to the mean beam momenta. The width of a peak is mainly determined (for pions) by the beam angular divergence and iris opening and (for protons) by the momentum spread. All of these quantities are relevant to the accurate calculation of flux. The index of refraction and counter resolution function are measured with 200-GeV protons extracted from the main accelerator.

2.2.3  ABSOLUTE INTENSITY   A combination of devices has been used to measure the number of secondary particles in the Fermilab decay pipe. At two different locations, helium-filled ionization chambers measured signals proportional to the beam intensity. (The choice of gas was influenced by small $dE/dx$ pion-proton differences and the absence of saturation effects.) The ion chambers were calibrated in four different ways. A 200-GeV beam of protons from the accelerator was transported through the secondary beam line (with the target removed) into the decay pipe where this intensity was simultaneously measured with several devices. The first method consisted of integrating the ion chamber output current while exposing Cu foils that were subsequently counted for $Na^{24}$ content. From the $Na^{24}$ activation cross section, previously measured at CERN (Chapman-Hatchett et al 1979), an ion chamber calibration was obtained. An independent measurement of this cross section was made at Fermilab, and it agreed well with the CERN

result: A second calibration used the rectified signal from a 53-MHz (beam structure frequency) rf cavity, located in the decay pipe to measure absolute intensity. The cavity's calibration depends primarily on the directly measured resonant frequency and quality factor. Finally a calibration was accomplished in a low-intensity beam where each particle was counted with standard detectors and circuitry. All of these ion chamber calibrations agree to within 3%, when measured differences of $6\frac{1}{2}\%$ between proton and pion ion chamber response are taken into account. These differences can be understood from calculations showing that secondary beam interactions in the ionization chamber foils are different for pions and protons, and that these interactions produce heavily ionizing nuclear fragments (Rapidis et al 1981).

2.2.4  MUON FLUX  The CERN technique of measuring the muon flux involves the use of small solid-state counters distributed at different depths in the muon shield downstream of the decay pipe (Mount 1981). From these counters the relative $\pi$-decay muon intensity is known as a function of radius and depth (Shultze 1977, Wachsmuth 1977). The shapes of the distributions, shown in Figure 13, reflect the dominance of multiple scattering in all but the first gap, where there is some sensitivity
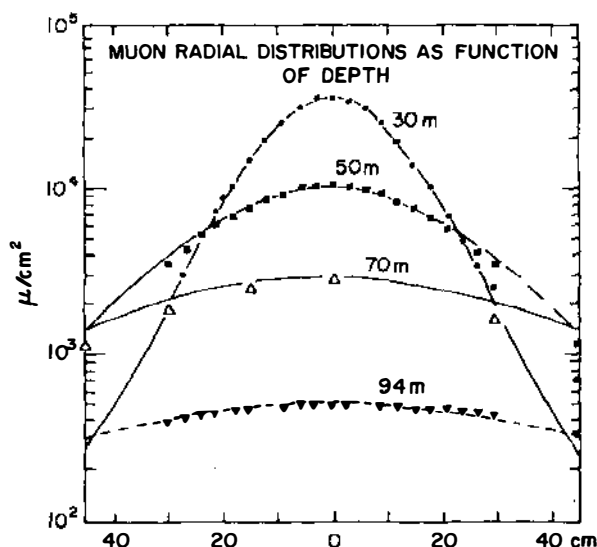


Figure 13  The distribution of muons from the CERN narrow-band beam at several depths in the shield. The peak is due primarily to muons from pion decay in the decay pipe (Shultze 1977).

to the angular divergence of the secondary beam. The solid-state counters seè all forms of ionization, including secondaries from up-stream interactions in the shield, cosmic rays, etc. Hence, an absolute calibration is required to obtain the absolute intensity of muons. This was accomplished by counting tracks in nuclear emulsion exposed in the same location as one of the solid-state counters. A plot of the angular distribution of these tracks exhibits a large forward peak $(\theta < 20 \text{ mrad})$, which, when compared with the background from knock-on electrons and cosmic rays at larger angles $(20 < \theta < 250 \text{ mrad})$, gives the fraction of the solid-state counter signal that is due to $\pi$-decay muons alone (Perkins 1978). The number of $\nu_\pi$ is then calculable, assuming that the signal/background in the counters is independent of radial position and beam setting.

The Fermilab groups are presently trying to measure the muon flux using segmented ion chambers, which can be calibrated in a known-intensity muon beam. This should provide a necessary redundancy for the entire question of neutrino flux measurement.

## 2.3  Detectors

Our present understanding of the weak interaction and the intent to study charged-current nucleon structure lead to several requirements for a neutrino detector: (a) sizeable mass from cross-section considera-tions; (b) muon detection for the identification of charged-current events; and (c) energy measurement of the hadrons and muons, and muon angle measurement for determining the values of the relevant variables $(x, y, Q^2)$ for individual events. Both bubble chamber and counter experiments, with appropriate beams, have been used to accumulate $\nu$, $\bar{\nu}$ data.

2.3.1  BUBBLE CHAMBER EXPERIMENTS  The bubble chamber experi-ments have employed hydrogen, deuterium, Ne-$H_2$, and propane-freon mixtures as the active target liquids. Typical fiducial mass for the Fermilab 15-ft bubble chamber or BEBC range from about one ton for hydrogen to twelve tons for a 74% molar Ne-$H_2$ mix in BEBC. The neon mix, in addition to providing extra tonnage, has a short radiation length, which permits efficient detection of electrons. This, for example, has been important in studies of charm production. The detection and identification of muons is accomplished primarily with external muon identifiers (EMI). The BEBC EMI consists of two planes of PWC's following 15 collision lengths of iron. It identifies muons whose mo-menta are greater than 10 GeV/$c$ with 98% efficiency (Brand et al 1978, 1982, Beuselinck et al 1978). The Fermilab EMI was reconfigured in

1977 into two PWC planes, following 3 to 5 pion absorption lengths. At the same time, an array of drift chambers internal to the bubble chamber vacuum vessel was added and this significantly improved the detection of dimuon events (Cence et al 1976, Stevenson 1978). Muon momentum resolution for the bubble chambers is typically 4–5% for 100 GeV/$c$ muons, while the rms error on hadron energy, $E_H$, is 20%. The value of $E_H$ for an event is determined by measuring all visible charged particles plus neutrals that interact. A correction for unmeasurable hadron energy of order 20% is applied to all events. The approximate magnitude of this correction is common to the CERN and Fermilab experience. It comes from the inability, in complicated events, to uniquely associate visible gamma rays and neutrons with a primary vertex. Checks on this correction, obtained by the transverse momentum balance technique, have been carried out using $\pi^-$ beams into the bubble chamber, as well as by comparing the measured event energy with that expected in narrow-band beam experiments (Bosetti et al 1978).

## 2.4 Counter Experiments

The counter experiments designed to investigate charged-current neutrino physics have three major components: target, calorimeter, and muon spectrometer. The calorimeter provides a measurement of the hadronic energy by sampling the energy deposition throughout the cascade shower downstream of the vertex. For all but the emulsion experiment (discussed in Section 3), the target and calorimeter are combined with tracking chambers to provide the above requirements. In Table 4, the basic properties are given for the CDHS, CHARM, HPWFOR, Fermilab E 594, and CFRR neutrino detectors, all of which have been used to collect deep inelastic neutrino scattering data. We do not discuss here other counter neutrino detectors at Brookhaven, CERN, Fermilab, LAMPF, and various reactors designed specifically to investigate $\nu_\mu$ and $\nu_e$ interactions at energies below the deep inelastic regime.

2.4.1 CFRR DETECTOR The experimental arrangement for the CFRR detector is shown in Figure 14. The calorimetry (for measurement of hadronic energy, $E_H$) is accomplished by recording the pulse height from light produced by the hadron shower in liquid scintillation counters (Barish et al 1975). Each counter, 3 m $\times$ 3 m $\times$ 2.5 cm, is a lucite box containing primary scintillator and wavelength shifter chemicals dissolved in a mineral oil base. Along the four edges of the counter and separated optically from it by an air gap, there exist wavelength shifter bars that collect light, shift it from blue to green, and transmit it to

**Table 4** Neutrino counter experiment apparatus summary

| Experiment | Tonnage (metric tons) and target material | Calorimetry type/resolution | Tracking $\theta_\mu$ type/resolution[a] (mrad/$P_\mu$) | $P_\mu$ resolution (%) | Average density (g cm$^{-3}$) |
|---|---|---|---|---|---|
| CDHS | 1400 Iron | Fe + plastic scint. (5-cm sample) $0.70E_H^{-1/2}$ | Drift chambers 150 | ±9 | 5.2 |
| CHARM | 170 Marble | Plastic scint. + proportional counters $0.53E_H^{-1/2}$ | Proportional drift tubes 70 | ±16 | 1.3 |
| HPWFOR | 385 Fe Fe + Scint Liq. Scint. | Fe + scint. $1.7E_H^{-1/2}$ Liq. scint. $0.7E_H^{-1/2}$ | Optical spark chambers Unpublished | ±12 | 7.9 3.0 0.8 |
| Fermilab E 594 | .340 Sand + Fe Shot | Flash chamber Hits $0.8E_H^{-1/2}$ | Flash chambers 70 | ±12 | 1.4 |
| CFRR | 1000 Fe + Scint. | Liq. scint. $0.89E_H^{-1/2}$ (10-cm sample) | Magnetostrictive spark chambers 35 | ±11 | 4.0 |

[a] Projected angular resolution for tracks outside of hadron showers. Resolution at the event vertex, which is more relevant, is not quoted here.
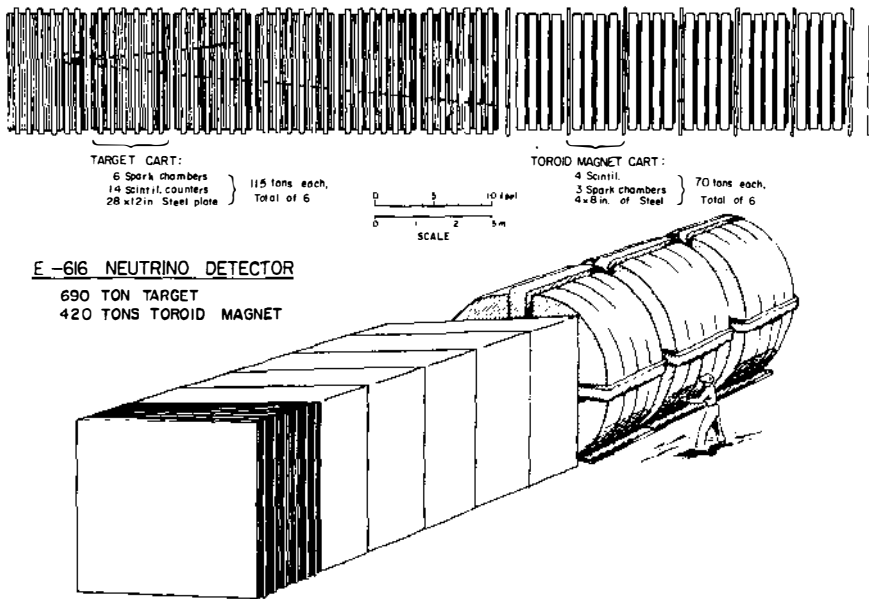
*Figure 14* The CFRR detector in Fermilab's Lab E. The steel target region is instrumented with counters and spark chambers to detect the interaction point and to track the muon downstream. The toroids permit measurement of final state muon momenta.

photomultipliers located at each corner of the counter (Barish et al 1978a). In this manner, hadron showers are sampled every 10 cm of Fe. After appropriate addition of all the pulse heights in a shower, $E_H$ is obtained with a fractional error of $0.89E_H^{-1/2}$ (Blair 1982). The individual counters yield ~10–15 photoelectrons for a minimum ionizing particle, which means that a threshold is easily set to signal the passage of a single muon for triggering purposes. In all, there are 82 planes of liquid counters in the CFRR target calorimeter.

Muons from neutrino interactions are identified and their position is determined by $3.2 \times 3.2$ m$^2$ magnetostrictive readout spark chambers. The 37 target spark chambers provide horizontal and vertical coordinates every 20 cm of Fe. To provide good multiple track efficiency, each chamber is individually pulsed in a transmission line mode with a 5-kV, 200-ns pulse across the 1.25-cm gap between plates. The spatial resolution of the chambers is ~0.5 mm. This implies that the projected muon angle error is 35 (mrad)/$P\mu$ (GeV) for muon tracks in which positions are measured in all chambers beginning at the vertex. In operation, hadron showers often mask the position measurement in the first chamber so that the actual angular resolution at the vertex is

approximately twice this value $(70/P_\mu)$ in the CFRR experiment. The degree of muon visibility after the vertex, which always compromises angular resolution, depends highly on the experiment.

The muon momentum is measured in a downstream group of instrumented toroids. The toroid spectrometer consists of 24 planes of acrylic scintillator for calorimetry and triggering, 37 spark chambers $1.5 \times 3.0$ m, and 4.9 m of magnetized iron for muon momentum determination. In addition, there are three separate banks of scintillators for muon triggering and time-of-flight measurements. Muons traversing the length of the spectrometer have a fractional momentum error of 11%, which is largely determined by multiple scattering.

With the typical errors discussed above for the CFRR experiment, the $x$ resolution can be calculated. Two examples are given in Figure 15, where it is noted that for small $x$ ($x = 0.05$) the $x$ resolution at small and large $y$ is dominated by the error on the muon angle, while the large-$x$
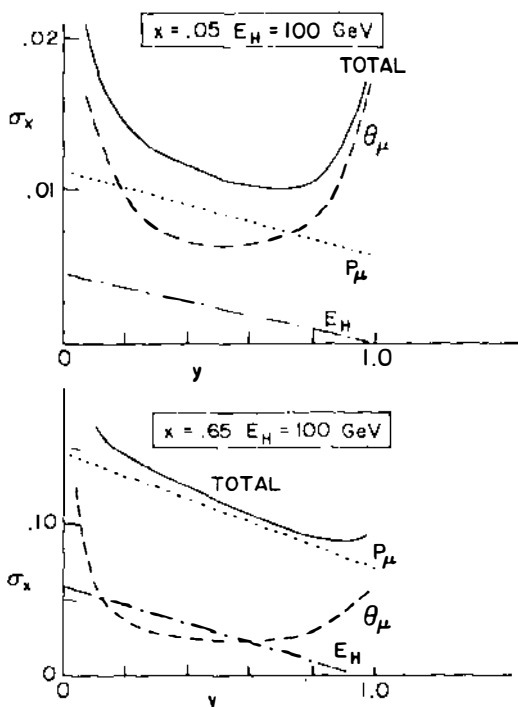


*Figure 15*   Examples of resolution on the $x$ variable $(\sigma_x)$ in the CFRR detector. At low $x$, the resolution on muon angle is most important; at large $x$, energy resolution is dominant. (Note difference in scale for $\sigma_x$.)

resolution is dominated by the muon momentum error. These resolutions produce systematic effects on structure function data that are similar in magnitude to the effects of Fermi motion in an iron nucleus.

2.4.2 OTHER DETECTORS   In the CDHS detector, all the iron is magnetized and thus provides for measurement of the muon momentum throughout the detector (Holder et al 1978). The measurement of track position comes from 19 large planar drift chambers with $y$, $u$, $v$ wire orientation (Marel et al 1977). Calorimetry is accomplished by sampling at 5- or 15-cm intervals of Fe (Abramowicz et al 1981). In total, there are 145 planes of NE 110 scintillator (5 mm thick) with each plane consisting of 8 counters and 16 photomultipliers. The resolution achieved (Abramowicz et al 1981a) with 15(5)-cm sampling is $1.35E^{-1/2}(0.70E^{-1/2})$. This represents an improved resolution that is obtained by weighting of the individual counter readouts using a technique previously employed (Dishaw et al 1979) with an iron calorimeter at Fermilab, where the improvement obtained was considerably less dramatic. The CFRR calorimetry data also show very little improvement by employing weighting techniques.

The CHARM detector (Diddens et al 1980) was developed primarily to study neutral-current interactions. It is a fine-grained calorimeter that can measure hadron shower energy and direction. The fiducial mass of the detector is derived from 8-cm thick marble slabs, which give approximately equal lengths for hadronic and electromagnetic showers. Surrounding the marble and scintillator center of the detector is an iron frame magnetized for measurement of muons leaving the sides of the apparatus. Calorimetry for the showers that develop in the iron frame is accomplished by using proportional tubes extending through this frame (Bosio et al 1978). The target calorimeter is followed by toroidal iron magnets for measurement of the momenta of forward muons.

The HPWFOR detector, which has completed its experimental program, consisted of three separate regions of target and calorimeter followed by 3.6- and 7.2-m diameter muon spectrometers (Benvenuti et al 1977, 1978, Heagy et al 1981). The three regions of detector included: (a) solid Fe (250 mT), (b) liquid scintillator (45 mT), and (c) Fe and scintillator target calorimeter (90 mT). Tracking was done with wide- and narrow-gap optical spark chambers.

The Fermilab E 594 detector (Taylor et al 1978, 1980, Bogert et al 1982, Bofill et al 1982, Stutte et al 1981) is a fine-grained calorimeter built to study neutral currents and $\nu_\mu e$ scattering, and consequently has many of the same design objectives as the CHARM detector. It is constructed of 38 modules each of which contain 16 (4 each of $u$, $x$, $y$, $x$)

flash chambers (5-mm cell size) for a total of 304 $x$ horizontal chambers and 152 $u$ (+10°) and 152 $y$ (−10°) vertical planes. The mass of the detector is made by filling 1.6-cm thick acrylic extrusions alternately with sand and steel shot. Proportional tubes, which follow each flash chamber module, provide the ability to trigger the apparatus and also give an alternative measure of an event's hadron energy. The gas-filled flash cells that glow discharge through the ionization path after being pulsed with high voltage are read out using magnetostrictive techniques. Hadron energy and energy flow for an event are then determined by the cells that have been hit. Figure 16 shows the response of the detector to a 35-GeV electron and a 35-GeV $\pi^-$. Downstream of the flash chamber
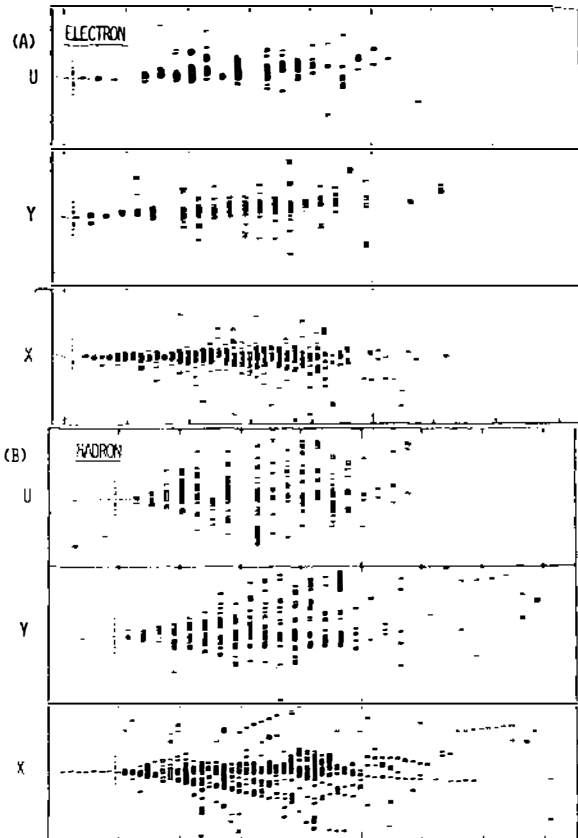


*Figure 16*  Response of the Fermilab Lab C neutrino detector to an electron and a hadron. The different transverse growth of the showers permits separation of electrons from hadrons in the final state of neutrino collisions.

target calorimeter are the muon spectrometer magnets built by the HPWFOR group, which consist of 3.6- and 7.2-m diameter toroids. The E 594 group has installed planes of proportional tubes for muon momentum measurement.

2.4.3    EVENT TYPES    All of the above detectors, using various arrangements for their trigger logic, can trigger on both charged- and neutral-current events. Examples of such triggers are shown in Figure 17.

# 3    TESTS OF THE QUARK MODEL AND DATA COMPARISONS

## 3.1    Total Cross Sections and y Dependence

An important test of the constituent quark model involves the energy dependence of the total cross sections ($\sigma^\nu$ and $\sigma^{\bar{\nu}}$). These should be nearly linear with respect to incident laboratory neutrino energy. The slope parameters, $\alpha^\nu = \sigma^\nu/E$ and $\alpha^{\bar{\nu}} = \sigma^{\bar{\nu}}/E$, are commonly used to refer to cross-section measurements. In the scaling limit, the sum and difference of these slope parameters for a target of equal numbers of neutrons and protons are given by

$$\alpha^+ \equiv \alpha^\nu + \alpha^{\bar{\nu}} = \frac{4}{3} \frac{G^2 M}{\pi} c' \int F_2(x) \, dx,$$

$$\alpha^- \equiv \alpha^\nu - \alpha^{\bar{\nu}} = \frac{2}{3} \frac{G^2 M}{\pi} \int x F_3(x) \, dx,$$

21.

where $F_2(x)$ and $xF_3(x)$ are defined in Table 3. The coefficient $c'$ includes a small correction for non-spin-$\frac{1}{2}$ ($R \neq 0$) and for the complications arising from the strange sea:

$$c' \equiv \left[ 1 + \frac{3}{4} R + \frac{1}{2} \int (s + \bar{s}) \, dx \middle/ \int (q + \bar{q}) \, dx \right] \middle/ (1 + R).$$

For the assumptions $R = 0.1$ (see Section 3.2) and $\int \bar{s} \, dx / \int (q + \bar{q}) \, dx = 0.025$ (see Section 4), these $2\frac{1}{2}\%$ effects exactly cancel ($c' = 1.00$).

The constancy of the cross sections divided by energy is an important test of the point-like constituency of nucleons. This test is obeyed within the accuracy of all measurements. For example, Figure 18 shows recent measurements by the CFRR group (Blair 1982, Rapidis et al 1981, Shaevitz et al 1981) of neutrino and antineutrino cross sections divided by energy ($\sigma^{\nu, \bar{\nu}}/E$), which are expected to be nearly constant. Although these data hint at a gentle rise with energy, the hypothesis of constancy
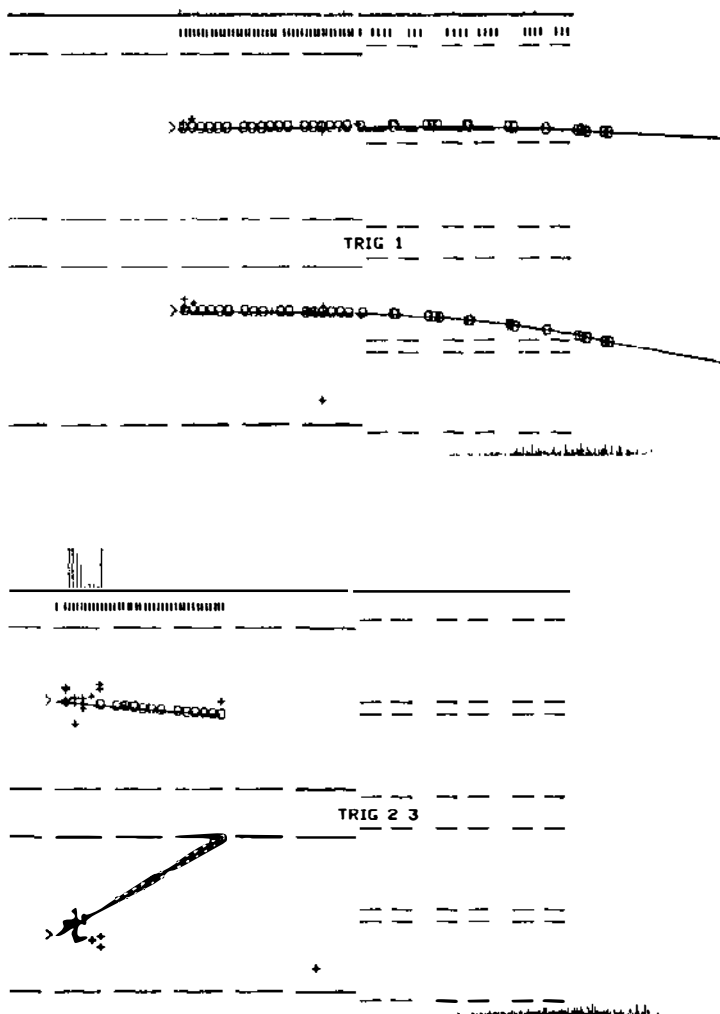
*Figure 17*  Neutrino charged-current interactions as recorded in the CFRR detector. Side and top views are shown for:

(*a*) event with very little hadronic energy and forward muon,

(*b*) event with very-wide-angle muon and considerable hadronic energy as sensed by the scintillation counters. The energy deposited in each counter is illustrated in the histogram at the top of the figure. The linear scale of energy deposition is calibrated with muons. Calibration of energy deposition vs hadronic energy is accomplished with a pion beam of known energy.
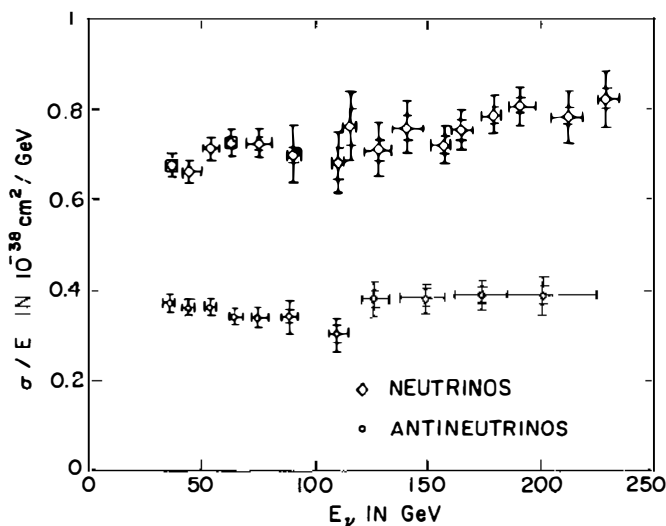
*Figure 18* Cross sections divided by neutrino energy from measurements by the CFRR group. This quantity is seen to be independent of energy within present errors. Such cross sections may be converted into integrals over the structure functions.

is acceptable within the errors. Earlier measurements (Barish et al 1977, Bosetti et al 1977, de Groot et al 1979) are also consistent with constant values of $\alpha$.

By utilizing Equation 21 and the values of $\alpha^\nu$ and $\alpha^{\bar\nu}$ shown in Figure 18, one can determine the fraction of momentum carried by interacting constituents. The result is $\int F_2\ dx = 0.512 \pm 0.018$ and $\int x F_3\ dx = 0.341 \pm 0.036$. In terms of fractional momentum carried by quark constituents, this is equivalent to $\int q(x)\,dx = 0.403 \pm 0.022$ and $\int \bar q(x)\ dx = 0.062 \pm 0.018$, and, by assumption, the remaining 10% is carried by non-spin-$\frac{1}{2}$ constituents ($R = 0.1$). One feature, dependent on the ratio of antineutrino to neutrino cross sections, is that the antiquark fraction is approximately 13–17% of the observed total. This number is generally agreed upon. It has been verified by the $y$ dependence of the cross section, where the relative dominance of quark over antiquark fraction should produce a nearly flat $y$ dependence for neutrinos, and an antineutrino cross section dominated by the $(1 - y)^2$ term (see Equation 9). Figure 19 shows this behavior explicitly for the CDHS data (Holder et al 1977, de Groot et al 1979), where the data indicate (assuming $R = 0$) that $\int \bar q\ dx/\int (q + \bar q)\ dx = 0.15 \pm 0.02$. Others observe very similar $y$ dependence, both qualitatively and quantitatively (e.g. Barish et al 1978, Bosetti et al 1978, Heagy et al 1981, Blair 1982). Precise agreement between these two techniques cannot be expected if the
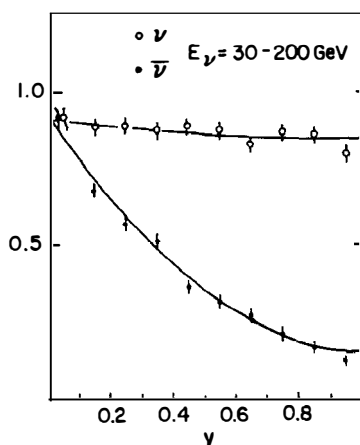
*Figure 19* The differential cross section vs $y$ for neutrinos and antineutrinos from CDHS data. The qualitative behavior of dominantly flat for neutrinos and dominantly $(1 - y)^2$ for antineutrinos is a feature anticipated in the quark model with valence quarks participating in the major portion of the scattering cross section. Similar behavior is observed in all neutrino experiments.

structure functions show explicit $Q^2$ dependence (see Section 3.6) or some finite $R$ value exists to change the $y$ dependence (see Section 3.2).

There is not, however, universal quantitative agreement on the magnitudes of the cross sections, and, therefore, on the net fraction of momentum carried by interacting constituents. The CFRR data of Figure 18 imply that the quarks carry 47% of the nucleon momentum, but older data imply less than 40% for this fraction. Table 5 shows a comparison of total cross sections obtained from several measurements. Here we see the discrepancy between the recent measurements of the CFRR group (Lee 1980, Blair 1982, Rapidis et al 1981, Shaevitz et al 1981) and older measurements (Barish et al 1977, Bosetti et al 1977, de Groot et al 1979), which average about 15% in the overall normalization and therefore in the fractional momentum as well. The last entry is a recent reanalysis of the BEBC data, incorporating a new flux calibration that employed muon detectors in the shield. One of these detectors was calibrated using emulsions to separate the muons of in-flight pion decay from extraneous background Section 2.2.3). This neutrino cross section lies between the others. There is agreement with the CFRR (Rapidis et al 1981) value of the integrated $xF_3$ value, but rather poor agreement on the sea contribution.

The discrepancy in normalizations is of some importance for the reasons discussed above, but also because it is directly related to tests of the mean-square charge of the interacting constituents (see Section 3.3). Since the experiments use different techniques for absolute $\nu$ flux normalization, efforts are under way to more precisely monitor flux and to incorporate aspects of the two techniques in all experiments (Rapidis et al 1981).

**Table 5** Measurements of cross-section slopes

| Reference | Energy range (GeV) | $\alpha^{\nu}$ [a] | $\alpha^{\bar{\nu}}$ [a] | $\int xF_3 \, dx$ | $\int F_2 \, dx$ | $Q$ | $\bar{Q}$ |
|---|---|---|---|---|---|---|---|
| Astratyan et al 1978 | 3–30 | 0.72±0.07 | 0.32±0.03 | 0.379±0.072 | 0.493±0.036 | 0.413±0.049 | 0.034±0.027 |
| Barish et al 1977 | 40–200 | 0.61±0.03 | 0.29±0.02 | 0.303±0.034 | 0.427±0.017 | 0.346±0.021 | 0.042±0.016 |
| Bosetti et al 1977 | 40–200 | 0.63±0.05 | 0.29±0.03 | 0.322±0.055 | 0.436±0.028 | 0.359±0.035 | 0.037±0.024 |
| deGroot et al 1979 | 30–200 | 0.62±0.05 | 0.30±0.02 | 0.303±0.051 | 0.436±0.026 | 0.350±0.035 | 0.046±0.019 |
| Jonker et al 1981 | 25–260 | 0.60±0.03 | 0.30±0.02 | 0.284±0.034 | 0.427±0.017 | 0.336±0.021 | 0.051±0.016 |
| Lee 1980 | 25–260 | 0.70±0.03 | | | | | |
| Rapidis et al 1981 | 30–230 | 0.70±0.03 | 0.35±0.023 | 0.331±0.036 | 0.498±0.018 | 0.392±0.022 | 0.061±0.018 |
| Fritze et al 1981 | 10–200 | 0.66±0.03 | 0.30±0.02 | 0.341±0.034 | 0.455±0.017 | 0.377±0.021 | 0.036±0.016 |

[a] Measured $\times 10^{-38}$ cm$^2$ GeV$^{-1}$.

## 3.2   *The* R *Parameter*

The prediction obtained by assuming spin-$\frac{1}{2}$ constituents (i.e. $R = 0$) is not expected to be exact, as discussed in the introduction. For example, at low $Q^2$, $R$ is expected to be nonzero (e.g. $R \sim 4\langle P_T^2 \rangle / Q^2$) and perhaps it has logarithmic dependence on $Q^2$ (from QCD effects) at higher energies. Thus far, measurements have not been very precise because they are exceedingly difficult to make. It requires extracting the $R$ parameter from $y$ distributions at fixed $x$ and $Q^2$. That is, the data should be divided among three variables, which makes statistical precision difficult. The systematic problems created by resolutions and radiative corrections are also very important.

Table 6 shows the average values of $R$ as obtained from two sets of neutrino data. Also shown are $R$ parameters obtained from ($\mu$, e) inelastic scattering. There is general agreement among all but the last entry (to which we return) that $R$ is small ($\lesssim 0.2$) on the average. The most recent measurement (Abramowicz et al 1981) is shown in Figure 20 as a function of $x$, averaged over $Q^2$. The data are not precise enough to be treated in these two variables separately, so they have been averaged over $Q^2$ at fixed $x$. This means that the low-$x$ data also are dominated by low $Q^2$ events. Tentatively then, the $R$ parameter

**Table 6**   Measurements of $R$

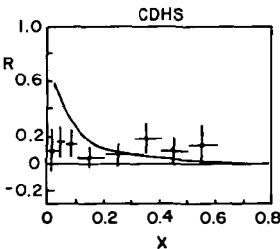| Group/Reference/Reaction | $x$ Range | $Q^2$ Range (GeV$^2$) | $R$ |
|---|---|---|---|
| BEBC/Bosetti et al 1978/$\nu$N | 0–1.0 | 0.1–50 | $0.15 \pm 0.10 \pm 0.04$ |
| CDHS/Abramowicz et al 1981/$\nu$N | 0–0.6 | 2.5–75 | $0.13 \pm 0.035 \pm 0.04$ |
| SLAC/Mestayer 1978/ep | 0.1–0.9 | 2–20 | $0.21 \pm 0.10$ |
| CHIO/Gordon et al 1979/$\mu$p | 0–0.1 | 1.5–12 | $0.52 \pm^{0.17}_{0.16}$ |



*Figure 20*   Experimental values of $R = \sigma_s/\sigma_T$ from neutrino scattering. A value of $R = 0.13$ independent of $x$ and $Q^2$ is consistent with the data (Abramowicz et al 1981).

shows no dramatic dependence on $x$ (or $Q^2$) and the qualitative features expected from QCD predictions do not appear. It is possible, of course, that the $R$ parameter gets contributions from more than a single source, which may make it difficult to draw definitive conclusions regarding QCD.

The last entry for $R$, obtained from muon scattering (Gordon et al 1979) on hydrogen, is specifically in the small-$x$ region. The dependence on small-$x$ values is shown in Figure 21a. This is somewhat reminiscent of the behavior expected from QCD, in the sharp falloff with $x$. It should be noted that the $Q^2$ in this small-$x$ region are quite low ($\lesssim 1$ GeV$^2$). The dependence on higher $Q^2$ is shown in Figure 21b, where the upper dashed curve parametrizes a $\ln Q^2/\Lambda^2$ dependence, and the other curve has a $1/Q^2$ dependence. The data cannot choose between them. The only neutrino data available with $x < 0.1$ (Figure 20) do not show any hint of large $R$ at small $x$. More information on $R$ in this small-$x$ region is clearly desirable both from muon scattering and from neutrino scattering. It is important to know whether the scattering is dominantly non-spin-$\frac{1}{2}$, as observed by CHIO, or whether the dominant spin-$\frac{1}{2}$ structure is preserved to very small $x$. If $R$ is large in this region, it is equally important to determine the $Q^2$ dependence; does it fall like a power of $1/Q^2$, or is it slower in its falloff and therefore has its origin in perturbative effects?

## 3.3 $F_2$ Structure Functions—x Dependence

The deep inelastic structure functions have been measured by several groups, which we designate BEBC (Bosetti et al 1978), CDHS (Eisele
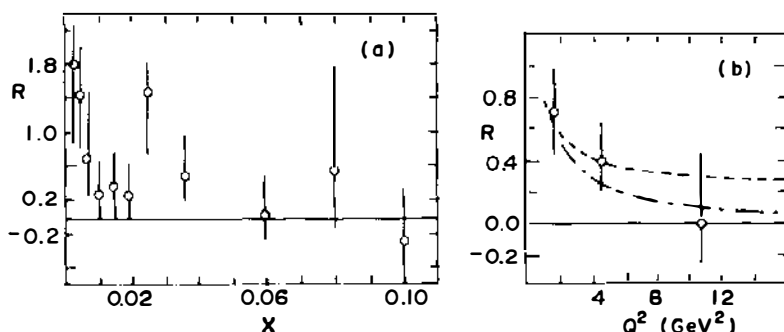


*Figure 21* Experimental values of $R$ from muon scattering on hydrogen by the CHIO group. (a) The very-small-$x$ region shows indication of a major enhancement in the non-spin-$\frac{1}{2}$ scattering. (b) The experimental values show a falloff in $Q^2$, but cannot differentiate between hypotheses of logarithmic falloff and power law falloff, illustrated by the two curves.

et al 1981, de Groot et al 1979, 1980) HPWF (Heagy et al 1981) and GGM (Morfin et al 1981). In this section, we discuss the qualitative features of this neutrino data, and make comparisons among the various data sets. Since an important prediction of the quark model relies upon the mean-square-charge test, i.e. a comparison of electron/muon structure functions ($F_2^{eN}$) with those from neutrino ($F_2^{\nu N}$), we also proceed to determine the consistency among several measurements of $F_2^{eN}$. Finally, we remark on the present level of agreement between weak and electromagnetic structure functions in the context of the quark mean-square-charge hypothesis. We postpone discussion of the $Q^2$ dependence (at fixed $x$) to a later section.

3.3.1   NEUTRINO STRUCTURE FUNCTIONS   The most statistically significant structure function data are those of the CDHS group (de Groot et al 1979, 1980, Eisele et al 1981). In particular, the latter data (more recent) employs a 120,000-event sample. Other groups use 5–10 times fewer high-energy events. The CFRR group has a high-statistics sample, from which structure functions are expected in 1982. Figure 22 shows the $x$ dependence of the $F_2$ and $xF_3$ values from the earlier CDHS data (de Groot et al 1979) averaged over the neutrino energy range, $30 < E_\nu < 200$ GeV. The curve utilizes the functional dependence described below with the exponents best fitted by their data; the overall
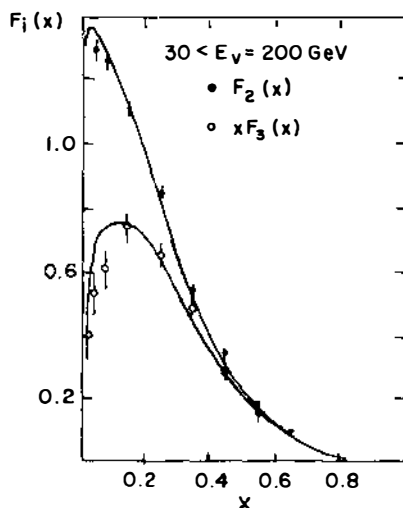


*Figure 22*   Qualitative features of the $x$ dependence of $F_2$ and $xF_3$ as seen in the early CDHS data, averaged over neutino energy. The curves drawn (Equation 22) are a reasonable representation of the qualitative behavior, especially at larger $x$ values.

normalization of the curve has been constrained by the GLS sum rule (see Section 1.7) and by the antiquark fraction, $\int \bar{q} \, dx / \int (q + \bar{q}) \, dx = 0.15$ (see Section 3.1). This parametrization assumes that $R = 0$ and

$$q(x) - \bar{q}(x) = 3\sqrt{x}(1 - x)^{3.5}/\beta(0.5, 4.5) \qquad 22.$$

$$\bar{q}(x) = 0.478 \ (1 - x)^{6.5}. \qquad 23.$$

This is a useful functional approximation. It conforms to these data shown for $x > 0.1$, but does not fit very well at lower $x$ values. The newer CDHS data (de Groot et al 1980, Eisele et al 1981) lie even lower at small $x$.

The other neutrino data sets have been compared directly to the new CDHS data to determine whether there are any significant differences. Figure 23 shows the comparison between BEBC and CDHS $F_2(x)$ in overlapping $Q^2$ ranges as a function of $x$. Since both groups obtained
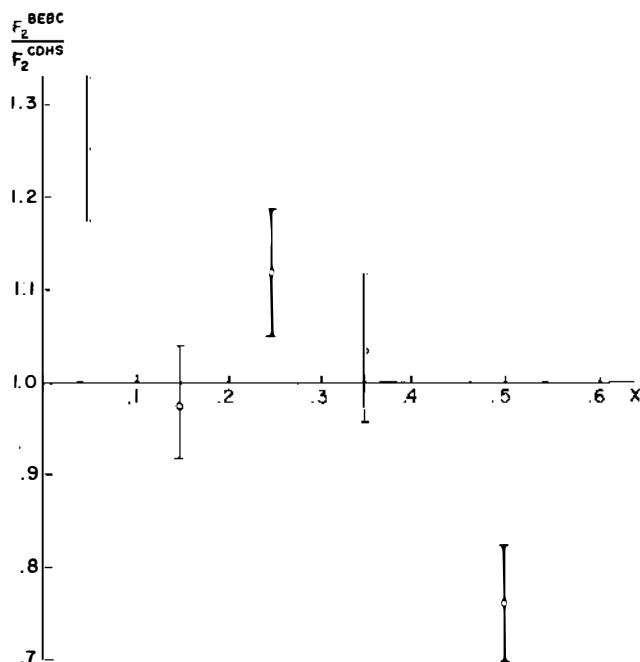


*Figure 23* Ratio $F_2$ (BEBC)/$F_2$ (CDHS) in the $Q^2$ range where the data overlap for these neutrino experiments. The error bars primarily reflect the statistical limitations in the BEBC data. The ratios at small and large $x$ indicate a qualitative shape difference between the data sets.

very similar total cross-section values, we expect little difference on the average, but we may find some shape differences. The BEBC data appear to be significantly higher at small $x$ ($x < 0.10$) and to have a smaller value of $F_2$ at large $x$ ($x \sim 0.5$). The BEBC structure function appears, therefore, to be more sharply peaked to small $x$ than does that of CDHS. This is a bigger effect than might be anticipated on the basis of Fermi-momentum correction effects between heavy liquid (BEBC) and iron (CDHS) targets (Bodek & Ritchie 1981). The GGM data show a similar, but less significant, behavior relative to CDHS. The HPWF data do not show it. We conclude that the $x$ distributions from neutrino scattering have the qualitative behavior vs $x$ as expressed in Equations 22 and 23; but there are some specific uncertainties: (a) the overall normalization has been measured to be different at approximately the 15% level (see Section 3.1); (b) the shape as observed in bubble chamber experiments is somewhat "sharper," showing differences of about 25% at small $x$ and at large $x$; and (c) a finite $R$ value affects the overall level of the quark and antiquark functions in proportion to its value. Although measurements of $F_2$ are largely independent of $R$, the magnitudes of the $q$ and $\bar{q}$ distributions do depend on $R$.

3.3.2  ELECTRON/MUON STRUCTURE FUNCTIONS   Several groups have measured electromagnetic structure functions (Bollini et al 1981, Aubert et al 1981, 1981a, Bodek et al 1979, Gordon et al 1979); the groups (targets) are BCDMS (carbon), EMC ($H_2$), EMC (iron), SLAC ($H_2$, $D_2$), and CHIO ($H_2$), respectively. The data with the highest statistical value and covering the greatest range of $x$ and $Q^2$ are those of the EMC group. We proceed to compare, where possible, the data of the various groups in the least biased manner. The most direct way to do this is to utilize $H_2$ data, which does not suffer from differing Fermi-motion corrections.

Figure 24 shows the comparison of $F_2$ vs $x$ for the data of CHIO (Gordon et al 1979) and EMC (Aubert et al 1981) over the same $Q^2$ range. The values of $F_2$ are obtained with the same assumption for $R$ ($R = 0.1$), although the qualitative features shown are not very dependent on this value. On the same graph is a comparison made independently (Smadja 1981) between SLAC (Bodek et al 1979) and EMC data. We perceive that the SLAC data lie systematically higher by about 10%, while the CHIO data are about 8% higher on average. The latter data indicate some $x$-dependence difference as well. The systematic errors in normalization (3–5%) quoted by these groups are similar to each other. To make the comparison between muon and neutrino scattering, we use the EMC data renormalized by the factor $1.06 \pm 0.06$.
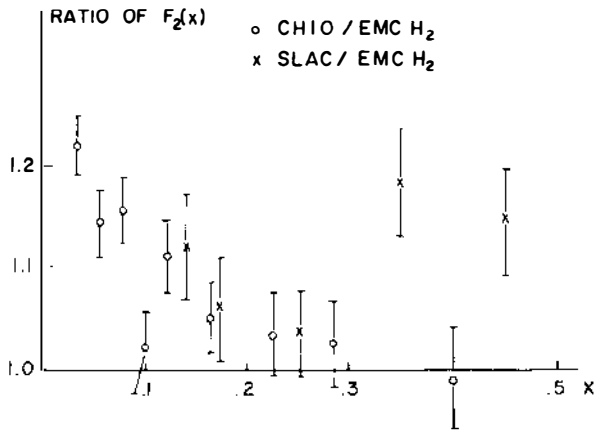
*Figure 24* Ratio of $F_2$ (CHIO)/$F_2$ (EMC) and $F_2$(SLAC)/$F_2$ (EMC) in regions of $Q^2$ overlap from these electron and muon experiments on hydrogen. The ratios have been obtained with the assumption $R = 0.1$ in the former comparison. The errors primarily reflect the errors quoted by the CHIO and SLAC groups. We assign an empirical renormalization factor, on the basis of these measurements, of $1.06 \pm 0.06$ to the EMC data for subsequent comparison.

This factor and its assigned error reflects an empirical uncertainty in normalization observed for the three experiments being compared.

3.3.3  TEST OF THE MEAN-SQUARE CHARGE    The $\nu$N structure function predicted by quark charges for $\mu$N scattering is given by

$$F_2^{\mathrm{pred}}(x) = \frac{\frac{18}{5} C F_2^{\mathrm{EMC}}(x)}{[1 - \frac{3}{5} s^{\mathrm{corr}}(x)]},$$
24.

where $C$ is the normalization parameter obtained in the last section, $C = 1.06 \pm 0.06$, and $s^{\mathrm{corr}}(x) = [s(x) + \bar{s}(x)/[q(x) + \bar{q}(x)]$ is the correction for strange sea. Here $q(x)$ and $\bar{q}(x)$ have been taken from Equations 22, and $s(x) = \bar{s}(x) = (0.2 \pm 0.1)\bar{q}(x)$, corresponding to $(50\% \pm 25\%)$ of an SU(3) symmetric strange sea ($\bar{s} = \bar{u} = \bar{d}$). The ratio $F_2^{\mathrm{pred}}(x)/F_2^{\mathrm{CDHS}}(s)$ is shown in Figure 25. This ratio should be unity at all $x$ if the hypothesis of the $\frac{5}{18}$ mean-square charge for quarks is to be corroborated by these data. Also shown in the figure is the uncertainty in $\mu$N normalization and the uncertainty in the strange-sea correction. At large $x$ ($x > 0.4$), the data are consistent with the 6% normalization uncertainties that we have assigned to the muon data. At smaller $x$, the discrepancy is greater than 20% for $x < 0.1$. This discrepancy cannot be explained by strange-sea assumptions and muon normalization uncertainties. In these terms, the difference could only be explained if the
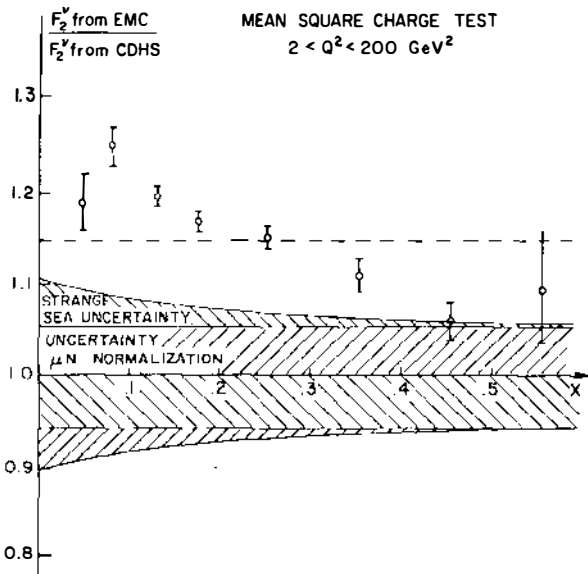
*Figure 25* The ratio of $F_2^\nu$ predicted by EMC muon data (on the basis of the mean-square-charge relation of Equation 24) divided by the $F_2^\nu$ measured by CDHS. Both data sets have the assumption $R = 0.1$. The ratio predicted in the quark model is 1.0, independent of $x$. Uncertainties on the muon data normalization and on the strange-sea correction are indicated. The dashed line corresponds to the quark model prediction if the neutrino cross section of CDHS were 15% higher.

charm sea were larger than the strange sea; this seems unlikely. The systematic discrepancy (i.e. all $x$ values lie above unity) may be related in part to the total cross-section controversy. If the neutrino data were renormalized upward by 15%, as indicated by the CFRR cross-section measurement, the quark model prediction would lie on the dashed line. This may help to resolve the systematic discrepancy; but there would still remain an $x$-dependent difference. The muon data show higher values at small $x$, lower values at large $x$; in other words, a distribution in $x$ that is considerably more peaked toward small $x$.

## 3.4 *The* $xF_3$ *Structure Function—x Dependence*

The $xF_3$ structure function is unique to neutrino scattering since it exists only because of the parity violation in the weak interaction. The integral of $F_3$ is important because it directly measures the valence quark composition of the nucleon. As with the $F_2$ structure function, both $x$ and $Q^2$ dependence are ●bserved for $xF_3$. We concentrate here on the

high-statistics data of the CDHS group (Eisele et al 1981). Systematic differences in the $x$ dependence when compared with data of other groups (Bosetti et al 1978, Heagy et al 1981, Morfin et al 1981) are qualitatively similar to those already discussed in Section 3.3.1 for the $F_2$ structure function.

The $Q^2$ dependence at fixed $x$ of $xF_3$ is rather similar to that of $F_2$, discussed in the next section. Here we concentrate on fixed $Q^2$, where the data can be satisfactorily fit to a functional form similar to Equations 22 and 23, i.e.

$$xF_3(x) = Cx^B(1-x)^A. \qquad 25.$$

Here $A$, $B$, and $C$ will, in general, depend on $Q^2$.

The qualitative behavior of these exponents has been anticipated from model arguments in the extreme low-$x$ and high-$x$ regions. At small $x$, the exponent $B$ dominates the behavior. From Regge theory, we expect $B$ will be directly related to the trajectory intercept ($\alpha$), which is dominant for $xF_3$: $B = 1 - \alpha$ (Reya 1981). Since $xF_3$ carries the nucleon's isospin, the highest contributing exchange is the $(\rho, \omega)$ trajectory with $\alpha \simeq \frac{1}{2}$. The next lowest trajectory is that of the $\pi$ with $\alpha \approx 0$, which would put $B$ in the range $\frac{1}{2} < B < 1$. The behavior near $x = 1$ is dominated by the exponent, $A$, where the predictions are based on counting rules and imply $A \approx 3$ to 4 (Gunion 1974, Farrar 1974).

Figure 26 shows the values of these exponents from fits to the CDHS data at fixed $Q^2$. The parameter, $A$, lies slightly below, but is consistent with the value three over this range of $Q^2$. The parameter $B$ falls from $\approx 0.65$ to $\approx 0.4$ over the $Q^2$ range between 2.5 and 25 GeV$^2$. A lower value of $B$ signals a more gentle rise with $x$, which could be an artifact due to the absence of very-small-$x$ data at higher $Q^2$.

## 3.5   The Gross–Llewellyn Smith Sum Rule

The GLS sum rule (see Section 1.7) is not expected to be exact, but is predicted to have perturbative QCD corrections at high $Q^2$ and possibly substantial power law dependence at low $Q^2$. To first order in perturbative QCD, we expect (Bardeen et al 1978)

$$S \equiv \int_0^1 F_3^{\nu N}(x)\, dx = \int_0^1 \frac{xF_3}{x}\, dx = 3\left[1 - \frac{12}{(33 - 2f)\ln Q^2/\Lambda^2}\right], \qquad 26.$$

where $f$ is the number of active flavors (3 to 4), and $\Lambda$ is the scale parameter of QCD, $\Lambda \approx 0.2$ GeV (see Section 3.6). Hence, we might expect a result roughly 5–10% lower than the nominal value at presently available $Q^2$.
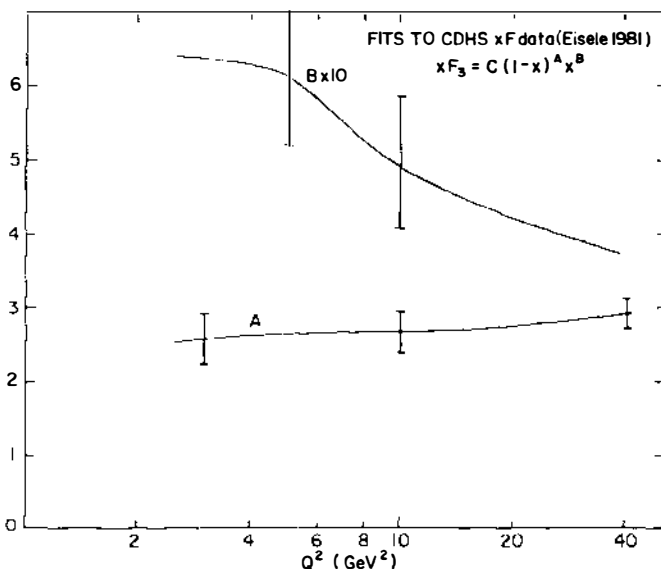
*Figure 26*  Values of the exponents from fitting CDHS $xF_3$ data to the indicated form.
Expectations are that $A$ would be around 3 to 4 and that $B$ would be between 0.5 and 1.

A determination of $S$ was made several years ago by the CDHS group
(de Groot et al 1979). They pointed out that the result depends
sensitively on the very-small-$x$ behavior of $xF_3$. By numerically integrat-
ing the data down to $x_{min} = 0.005$, they obtained $S_{x_{min}} = 2.7 \pm 0.3$.
Extrapolating from $x_{min}$ to zero, and using the fitted values in
Equations 22 and 23, gave $S = 3.2 \pm 0.5$ which dramatically illustrates
their point. A similar effect was reported earlier by the BEBC group
(Bosetti et al 1978).

Alternatively, we may use the values of $A$, $B$, and $C$ at fixed $Q^2$ found
by fitting the newer CDHS data discussed in the last section. From these
parameters and their covariance matrix, the integral $\int F_3 \, dx$ and its error
were calculated directly. Figure 27 shows the resultant integral over the
range $1 < Q^2 < 10$ GeV$^2$, where there exist data at small $x$. This
technique of finding the integral of $F_3$ also suffers from insufficient
knowledge in the small-$x$ region. Note that the value of the integral is
substantially lower than the prediction (Equation 26), which is also
shown in the figure.

In any case, in the $Q^2$ range where data exist at smaller $x$ values
($Q^2 < 10$ GeV$^2$), the sum rule result is very low. This represents a
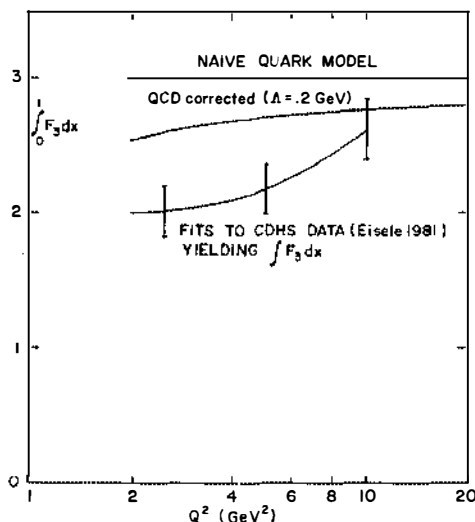problem at present. Its resolution may be found in one or more of the

*Figure 27* Experimental values of $\int_0^1 F_3 \, dx$ from fits of CDHS data of Equation 25. The values are somewhat lower than expectations.

following explanations: (a) The technique applied here is generally inferior to one in which the integration is performed on unbinned data. (b) A renormalization of the structure functions upward may occur because of a higher total cross section. (c) A shape difference with relatively higher structure function values at small $x$ would raise this integral. (d) A serious problem exists with the quark model.

An illustration of points (b) and (c) lies in a recent evaluation of this sum rule by the BEBC group (Fritze et al 1981). Their new cross-section measurements are such that the integrated value of $xF_3$ is higher than that from the CDHS data by 13% (see Table 5) and their values of $xF_3$ at small $x$ are considerably higher (illustrated by the $F_2$ comparison in Figure 23). Their evaluation of the sum rule is shown in Figure 28, which is by contrast even higher than the QCD corrected prediction. Clearly, this very critical test of the quark model requires some attention.

## 3.6   The $Q^2$ Dependence of Structure Functions at Fixed x

Scaling violations have been observed ever since approximate scaling was discovered (Miller et al 1972, Bodek et al 1973, Eichten et al 1973). Over the low-$Q^2$ regions ($Q^2 \lesssim 2$ GeV$^2$), the structure functions at fixed $x$ were found to vary by large factors. A better approximation to scaling

was found by using a new scaling variable, e.g. $x' = Q^2/(2M\nu + M^2)$, which approaches $x$ at large $Q^2$ (Bodek et al 1973). This is very similar in its effect to a $1/Q^2$ dependence of the structure functions.

Theoretical interest in the past few years has focused on perturbative QCD, which predicts that structure functions have an approximate logarithmic dependence on $Q^2$. Quantitative predictions can be made at any $Q^2$ by using the quark and gluon structure functions at a single value of $Q^2 = Q_0^2$ as input. The evolution of the distributions, in the leading order of a perturbation series, depends on a single scale parameter, $\Lambda$, measured in GeV. Higher-order corrections in the perturbation can also be calculated, but the $1/Q^2$ terms cannot. These depend on the bound-state wave functions of the quarks, which thus far have eluded calculation in the theory.

The principle uncertainty faced in confronting the predictions of QCD with experimental tests is that we do not know *a priori* where the perturbative (logarithmic) behavior begins to dominate over the bound-state effects. At some high $Q^2$, logarithmic dependence will dominate over power law (higher-twist) dependence. While we might naively presume that the higher-twist effects will disappear near energies corresponding to quark bound states ($\sim 1$ GeV$^2$), there could be bizarre $x$ dependences that amplify them (see Section 1).

Historically there have been proponents of the ansatz that perturbative behavior begins at very low $Q^2$. The only trustworthy empirical result that might corroborate the dominance of perturbative QCD behavior would be in the agreement of the parameter $\Lambda$ over a very large range of $Q^2$. The agreement of the data with the best-fit structure function curves and the agreement with prediction of the ratios of structure function moments have been touted as verification that the perturbative behavior has been seen. But there is reason to doubt the sensitivity of these tests as we discuss below.
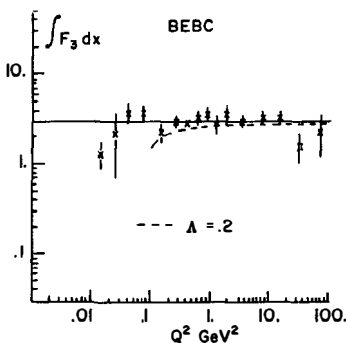


*Figure 28*    Values of $\int_0^1 F_3 \, dx$ quoted by the BEBC group over a large range of $Q^2$, using their most recent normalization (Table 5). These values are consistent with 3 at essentially all $Q^2$. Note the logarithmic scale for the ordinate.

Table 7 shows the values of $\Lambda$ obtained by various groups using neutrino and muon beams. The results have been obtained using three different techniques: (a) moment analysis (Nachtmann 1973), (b) the Buras-Gaemers prescription (Buras & Gaemers 1978), (c) evolution of the structure functions from a simple parametrization at $Q_0^2$ using the Altarelli-Parisi equations (Altarelli & Parisi 1977, Gonzalez-Arroya et al 1979, 1980). These procedures are described in detail by others (see, for example, Söding & Wolf 1981). The second technique (b) also evolves the structure functions in $Q^2$, but assumes a specific functional dependence on $x$ at each $Q^2$.

The first entry in the table was the earliest attempt at confrontation of perturbative QCD with experiment. Data were used that extended to very low $Q^2$ ($\sim 0.15$ GeV$^2$). The moment analysis technique seemed appropriate since the ratio of moments obtained from the data agreed with the predictions of QCD. There have been many criticisms of this technique since then (see, for example, Söding & Wolf 1981). However, we see that experiments using that technique or others obtain values of $\Lambda$ largely independent of the procedure. On the other hand, the ratio of moments test does not appear to be very sensitive to the source of the scaling violations.

The most striking feature from this table is the evolution in values of $\Lambda$: from over 700 MeV in 1978 down to 80–250 MeV most recently. The ratios of moments agreed with QCD predictions in all cases; the data were consistent with the theoretical fits in all cases. The change in the value of $\Lambda$ is primarily associated with the $Q^2$ range of the data used for the fitting. It seems unlikely, therefore, that the low-$Q^2$ data are described by the same QCD as that describing the high-$Q^2$ data.

As an illustration of this point, Figure 29 shows the $F_2$ data at $x = 0.5$ of BEBC (Bosetti et al 1978) and CDHS (de Groot et al 1980, Eisele et al 1981). For $Q^2 > 5$ GeV$^2$, the qualitative variation with $Q^2$ is similar. (The difference in normalization has already been mentioned in the discussion of Figure 23.) For $Q^2 < 5$ GeV$^2$, the BEBC data show a very pronounced rate of change. This is directly related to the large values of $\Lambda$ obtained when lower-$Q^2$ data are included in the fit.

The best and perhaps only test of perturbative QCD rests in the measured values of $\Lambda$ (in first order) or, more generally, in the value of the quark-gluon coupling, $\alpha_s(Q^2)$. We should obtain consistency for $\Lambda$ in muon and electron experiments and in $e^+e^-$ production of jets, etc. More importantly, the value of $\Lambda$ should not depend on the range of $Q^2$ used in the fit so long as the momentum transfers are high enough.

Values of $\Lambda$ in the range 100–200 MeV seem very reasonable for a scale of the strong interactions. Higher values have also been deemed

**Table 7**  Values of $\Lambda$ (GeV) obtained from fits to inelastic data

| Reference | Group | Reaction | Moments | Buras-Gaemers technique | Altarelli-Parisi technique |
|---|---|---|---|---|---|
| Bosetti et al 1978 | BEBC | $\nu N$ | $0.74\pm0.05$ GeV $(Q^2 > 0.15$ GeV$^2)$ | $0.47\pm0.1\pm0.1$ $(Q^2 > 3$ GeV$^2)$ | |
| de Groot et al 1979 | CDHS | $\nu N$ (Fe) | | | |
| Aubert et al 1981 | EMC | $\mu N$ (Fe) | | | $0.122^{+0.022+0.114}_{-0.020-0.070}$ $(Q^2 > 3.2$ GeV$^2)$ |
| Aubert et al 1981 | EMC | $\mu p$ (H$_2$) | | | $0.110^{+0.058+0.114}_{-0.020-0.070}$ $(Q^2 > 2.5$ GeV$^2)$ |
| Bollini et al 1981 | BCDMS | $\mu N$ (C) | $0.080^{+0.130+0.100}_{-0.080-0.070}$ $(Q^2 > 25$ GeV$^2)$ | $0.136^{+0.050+0.090}_{-0.040-0.080}$ $0.3 < x < 0.7$ | $0.085^{+0.060+0.090}_{-0.040-0.080}$ |
| Eisele et al 1981 | CDHS | $\nu N$ (Fe) | | | $0.19\pm0.08$ $(Q^2 > 2$ GeV$^2)$ $(W^2 > 11$ GeV$^2)$ |
| Fritze et al 1981 | BEBC | $\nu N$ | $0.245^{+0.130}_{-0.145}$ $(Q^2 > 1.5$ GeV$^2)$ | | $0.210\pm0.095$ $(Q^2 > 2$ GeV$^2)$ |
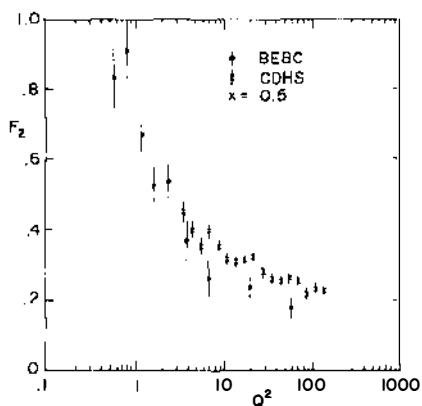
*Figure 29* Comparison of BEBC and CDHS $F_2$ data at $x = 0.5$. The behavior below $Q^2 = 5\,\text{GeV}^2$ in the BEBC data shows very strong dependence on $Q^2$.

reasonable. One source of concern is whether $\Lambda$ will continue to grow smaller as data become better and extend to higher $Q^2$. It will be peculiar if bound states of quarks are characterized by radii of order $(m_\pi c/\hbar)^{-1} \approx (140\ \text{MeV})^{-1}$, and the distance scale of the force were to be significantly longer than this.

For the experimentalist, the problem is a difficult one. The experiments represented in the last five entries of Table 7 generally have values of $\Lambda$ consistent with 200 MeV, but with some variation around this value. The differences in quoted values of $\Lambda$ are directly attributable to differences in the behavior of the data, particularly at high $x$. All techniques, especially the moments analysis and the Altarelli-Parisi evolution, give very consistent answers, so differences in analysis procedure are not likely to be producing different $\Lambda$ values. As an illustration that the $\Lambda$ values are closely related to the raw data, Figure 30 shows a slope parameter, $b(x)$, defined by fits to the functional form

$$F_2(x, \ Q^2) = A(x)[1 + b(x) \ \log_{10}(Q^2/10)].\qquad\qquad 27.$$

The slope parameter $b(x)$ is approximately $\Delta F_2(x)/F_2(x)$, or the fractional change in $F_2$, over a decade in $Q^2$. The data points are from the BCDMS ($\mu$N), EMC ($\mu$N), and CDHS ($\nu$N) groups, respectively. The curves have been drawn to guide the eye. At small $x$ ($\lesssim 0.2$), the two groups of data show very similar behavior. At large $x$, where muon and neutrino results should be dominated by the same valence quark distribution, there are systematic differences in the change in $F_2$ per decade. These are directly correlated with the $\Lambda$ values obtained by the groups: larger $\Lambda$ is associated with more negative values of $b$. It should be noted that the error bars shown for the EMC data are statistical only. At the present level of precision, the experimenters agree that the differences in $\Lambda$ are consistent within systematic and statistical errors.
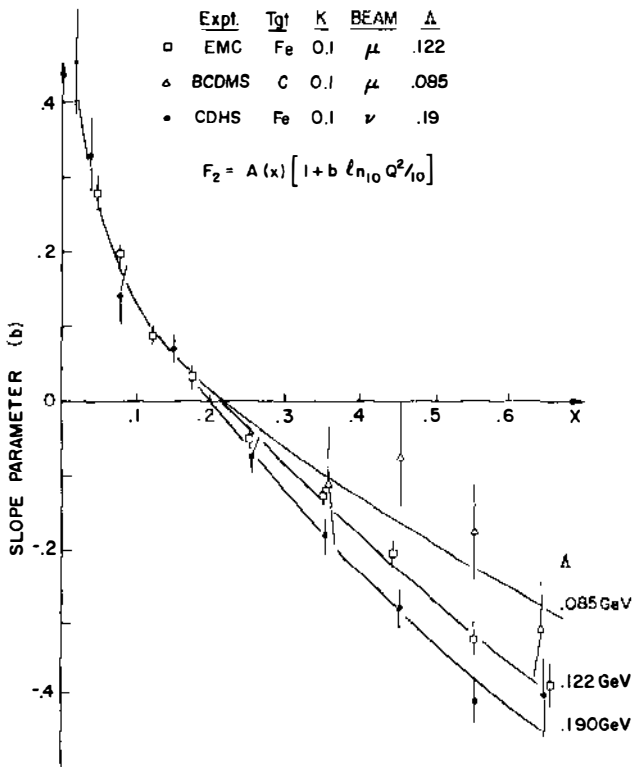
*Figure 30*  Slope parameter vs $x$ over similar $Q^2$ ranges from three different experiments. The curves have been drawn to guide the eye only. The best values of $\Lambda$ obtained in QCD fits are indicated. Differences in $\Lambda$ are correlated with different systematic logarithmic behavior at large $x$ in the raw data.

With small values of $\Lambda$ generally agreed upon, there is a critical challenge to be met. This is to obtain high-statistics muon and neutrino inelastic data with the greatest possible precision and over the widest possible range of $Q^2$, so that the value of $\Lambda$ can be measured accurately. The extension of the $Q^2$ range is crucial: if the value of $\Lambda$ continues to shrink, perturbative QCD will be in question.

# 4.  PRODUCTION OF CHARM AND NEW FLAVORS

## 4.1  *Introduction*

The four-quark theory of Glashow, Illiopoulos, and Maiani (Altarelli et al 1974, Gaillard 1974, Glashow, Illiopoulos & Maiani 1970) permitted

predictions of the rate for deep inelastic neutrino production of charm to be made quite early (Altarelli et al 1974, Gaillard et al 1974). (For a theoretical review, scc Gaillard, Lee & Rosner 1975.) These gave impetus to experimental searches for neutrino-induced charmed particles.

As discussed in Section 1.6, the production of charm with its subsequent semileptonic decay leads to final states with two opposite-sign leptons, and it was in fact the observation of such dimuons early in 1974 that gave the first experimental hint of charm (Rubbia et al 1974).

Owing to the short lifetimes, $\sim 10^{-13}$, of charmed mesons and baryons, the conventional bubble chamber spatial resolution has not permitted the systematic observation of charmed particle tracks before they decay. Bubble chamber groups have studied some specific charmed states, using traditional techniques of invariant mass peaks for final-state particles. These searches look for weakly decaying charmed mesons like $D^+$ $(c\bar{d})$, $D^0$ $(c\bar{u})$, $F^+$ $(c\bar{s})$, and the baryon $\Lambda_c^+$ (cud), as well as looking for the strongly decaying higher states.

Since inclusive charm production from neutrino and antineutrino beams is primarily related to the strangeness content of the nucleon (see Section 1.6), the study of dileptons in both bubble chamber and counter experiments provides information on the strength and $x$ dependence of the strange-quark sea.

## 4.2 Resonant States

In order to definitely demonstrate that a new flavor has been found, it is not sufficient to see resonances in a mass plot. Historically (e.g. with strangeness) the most compelling demonstrations have included (a) a state long-lived enough to see a separation between production and decay, and/or (b) a violation of a selection rule well established for existing flavors. The first explicit observation of charm production and decay, which occurred shortly after the discovery of $J/\psi$, involved the second of these. The BNL group observed a single event due to the reaction $\nu_\mu p \rightarrow \mu^- \Lambda^0 \pi^+ \pi^+ \pi^+ \pi^-$, which violates the sacred $\Delta S = \Delta Q$ rule for semileptonic weak interactions (Cazzoli et al 1975). We now attribute this to the process $\nu_\mu + p \rightarrow \mu^- + \Sigma_c^{++}$ and subsequent decays $\Sigma_c^{++} \rightarrow \Lambda_c^+ + \pi^+$ and $\Lambda_c^+ \rightarrow \Lambda^0 \pi^+ \pi^+ \pi^-$. This discovery was followed by the observation in a Fermilab emulsion experiment of a 182-$\mu$m track that very likely was a charmed particle, although the decay could not be uniquely identified (Burhop et al 1976).

Many examples of charmed particle decays have since been observed in bubble chamber experiments, where mass peaks are directly

correlated with charmed-particle mass peaks seen from $e^+ e^-$ collisions. In many cases, these neutrino events demonstrate through their violation of strangeness and isospin selection rules that a new flavor is involved. Table 8 shows a summary of these results.

Several experimental groups have recently attempted to use emulsion stacks in neutrino beams to exploit the above-mentioned property (a) of finite distance between production and decay. Besides providing a very clean signature for weakly decaying charmed particles, this promises quantitative determination of their lifetimes (or absolute total decay rates). Six such events were reported by a BEBC group (Angelini et al 1979a, b, Allasia et al 1979) and one apparently unique $F^+ \rightarrow \pi^+ \ \pi^+ \ \pi^- \ \pi^0$ by the Fermilab group (Ammar et al 1980).

At Fermilab, the E 531 hybrid emulsion experiment has accumulated the largest existing sample of charmed-particle states, with masses, lifetimes, and decay modes measured (Ushida et al 1980a, b). They used 23 liters of emulsion as target for the detector shown in Figure 31. By searching the emulsion for vertices predicted from the drift chamber tracks, they found 23 charged and 21 neutral multiprong short-lived decays. The emulsion was exposed to neutrinos in a single-horn, wide-band beam produced by 350-GeV protons (Ushida et al 1980b). A photomicrograph of an $F^-$ production event is shown in Figure 32. Kinematic fitting of the E 531 candidates and a single F candidate from another experiment (Ammar et al 1980) leads to the information on the 34 events listed in Table 9.

**Table 8**   Charmed particles identified in bubble chamber neutrino experiments[a]

| Experiment | D | $\Lambda_c^-$ | $\Sigma_c$ | D* |
|---|---|---|---|---|
| Baltay et al 1978 | 64/180 | | | |
| Baltay et al 1979 | | | 20/6 + + | |
| Cnops et al 1979 | | 2/0 | | |
| Grassler et al 1981 | | 2/0 | | |
| Blictschau et al 1979 | | | | 2/0 + |
| Kitagaki et al 1980 | | 19/10 | | |
| Kitagaki et al 1982[b] | | 1/0 | 2/0 | |
| Armenise et al 1981 | | 51/16[c] | | |

[a] Number of identified charm events/number of non charm background events is indicated. Charge mode is also indicated where appropriate.
[b] These three events have the decay mode $\Lambda_c^+ \rightarrow \Sigma^0 \pi^+$.
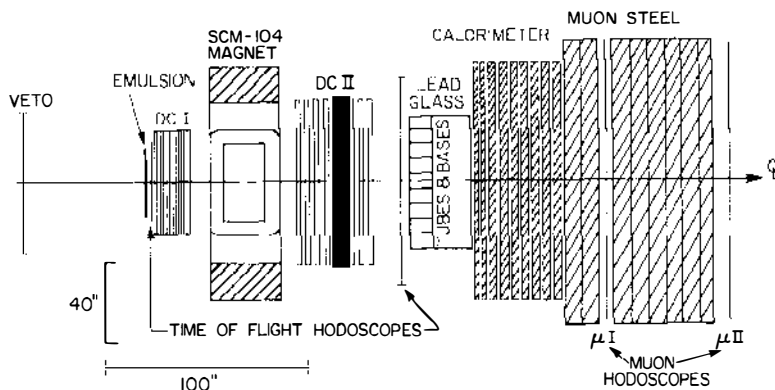[c] Inclusive $\Lambda_c^+$, $\Sigma_c^+$, and $\Sigma_c^{++}$ events.

*Figure 31*  E 531 experiment utilizing 23 liters of emulsion target. The momenta of secondary charged particles are measured using the drift chambers DCI, DCII, and the SCM 104 magnet. The time-of-flight hodoscopes are used for charged-particle identification. There is Pb glass for e and $\gamma$ identification ($\Delta E = \pm 0.14\ E^{1/2}$) and a hadron calorimeter for identification of neutral hadrons. Muons are identified by their passage through steel.

Note that there are included a single $D^-$, a single $F^-$, and three $\bar{D}^0$ events in Table 9 that are accompanied by a $\mu^+$. This implies that they are produced by incident antineutrinos. The $\nu/\bar{\nu}$ beam flux estimates agree with the observed $D/\bar{D}$ production ratio; this is consistent with the absence of short-lived mixing of these charmed mesons, in contrast to the analogous strange-particle case where $K^0/\bar{K}^0$ mixing is complete.

The table also indicates the observed decay modes and aggregate lifetimes and shows the predominance of charmed meson production
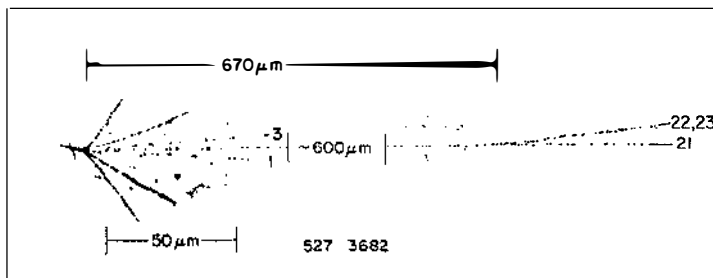


*Figure 32*  Photomicrograph of an E 531 $F^-$ event. The figure shows the result of an antineutrino interaction in emulsion that produces a 12.8-GeV $F^-$ meson ($\bar{c}s$ quark state). The $F^-$ is accompanied by a 30.3-GeV $\mu^+$ (track 1) and a 5.1-GeV positive track (track 3). The $F^-$ decays after 670 $\mu$m to a 5.4-GeV $\pi^-$ or $K^-$ (track 21), a 1.5-GeV $\pi^-$ (track 22), a 1.1-GeV $\pi^+$ (track 23), and a 4.8-GeV $\pi^0$, which has two measured $\gamma$'s. The two-constraint fitted $F^-$ mass is $2.026 \pm 0.056$ GeV/$c^2$ and the decay time is $3.6 \times 10^{-13}$ s.

**Table 9**  E 531 emulsion experiment event data

| $A_c$[a] | F |
|---|---|
| $\Lambda_c^+ \to p\bar{K}^0$ | $F^- \to \pi^+\pi^-\pi^-\pi^0$ |
| $pK^-\pi^+\pi^0$ | $F^+ \to K^+\pi^!\pi^+\pi^-\bar{K}^0$ |
| $p\pi^+\pi^-\bar{K}^0$ (2)[b] | $\to K^+K^-\pi^+\pi^0$ |
| $\Lambda\pi^+\pi^-\pi^+$ (3)[b] | $\to \pi^+\pi^+\pi^-\pi^0$[c] |
| $\Sigma^0\pi^+$ | |
| | $M_F = 2042 \pm 33$ |
| $M_{\Lambda_c} = 2265 \pm 30$ | |
| $\tau_{\Lambda_c} = 1.4 \, ^{+0.8}_{-0.4} \times 10^{-13}$ s | $\tau_F = 2.0 \, ^{+1.8}_{-0.8} \times 10^{-13}$ s |

| $D^0$ or $\bar{D}^0$ | $D^+$ or $D^-$ |
|---|---|
| $D^0 \to K^-\pi^+\pi^0$ | $D^+ \to K^-\pi^+\pi^+\pi^0$ |
| $K^-\pi^+\pi^0\pi^0$ | $\to K^-K^+\pi^+\pi^0$ |
| $K^-\pi^+\pi^-\pi^+$ (2)[b] | $\to K^-\pi^+e^+(\nu)$ |
| $K^-\pi^+\pi^-\pi^+\pi^0$ (2)[b] | $\to K^-\pi^+\mu^+(\nu)$ |
| $K^-\pi^+\pi^+\pi^+\pi^-\pi^-$ | |
| $\bar{K}^0\pi^+\pi^-$ (2)[b] | $D^- \to K^+\pi^-e^-(\nu)$ |
| $\bar{K}^0\pi^+\pi^-\pi^0$ | |
| $\pi^+\pi^+\pi^+\pi^-\pi^-\pi^-\pi^0$ | $M_{D^\pm} = 1851 \pm 20$ |
| $K^-e^+\nu$ | $\tau_{\Lambda_{D^\pm}} = 10.3 \, ^{+10.3}_{-4.2} \times 10^{-13}$ s |
| $K^-\mu^+\nu$ | |
| $K^-\pi^+\pi^-\mu^+\nu$ | Summary |
| $\bar{D}^0 \to K^+\pi^-\pi^0$ | |
| $K^+\pi^-\pi^0\pi^0$ | 8 $\Lambda_c$ |
| $K^+\pi^-\pi^+\pi^-\pi^0$ | 4 F |
| | 5 charged D's |
| $M_{D^0} = 1842 \pm 16$ | 17 neutral D's |
| $\tau_{D^0} = 2.3 \, ^{+0.8}_{-0.5} \times 10^{-3}$ s | |

[a] 4 $\Lambda_c^+$ are consistent with having either a $\Sigma_c^{++}$ or $\Sigma_c^0$ parent.
[b] Indicates multiple candidates of a given type.
[c] This event is from E 564, Ammar et al (1980).

over that of charmed baryons (Stanton 1981). The $D^0$, $D^\pm$ lifetime results indicate that the $D^\pm$ lifetime is larger than that of the $D^0$ (Ushida et al 1982). Indirect evidence to this effect came from a comparison of the relative leptonic branching ratios of these states as measured in $e^+e^-$ collisions (Bacino et al 1980, Schindler et al 1981).

The production characteristics of the charmed mesons and baryons are different. These data and others (Armenise et al 1981) give evidence

for some production of charmed baryons with low $Q^2$. Armenise et al quote a quasi-elastic cross section times branching ratio for the total production of $\Lambda_c^+$, $\Sigma_c^+$, $\Sigma_c^{*+}$ to be $\sigma B = 14.3 \pm 7.4 \times 10^{-40}\,\mathrm{cm}^2$. Here the branching ratio $B$ refers to the probability to decay into neutral vees: $B = [\Gamma(\Lambda_c^+ \to \Lambda_0 + \ldots) + \Gamma(\Lambda_c^+ \to \bar{K}^0 + p + \ldots)]/\Gamma(\Lambda_c^+ \to \mathrm{all})$.    The number of similar E 531 candidates is consistent with this number. For scale, we compare this value of $\sigma B$ to the asymptotic cross sections for the quasi-elastic processes, $\nu n \to \mu^- p$ and $\nu p \to \mu^- \Delta^{++}$ of $\sim 90 \times 10^{-40}$ and $\sim 65 \times 10^{-40}\,\mathrm{cm}^2$, respectively (Mann et al 1973, Barish et al 1979). Theoretical estimates of the quasi-elastic charmed-baryon cross sections depend on how the SU(4) symmetry breaking and quark model with orbital excitations are handled (Finjord & Ravndal 1975, Schrock & Lee 1976, Avilez et al 1978, Amer et al 1979, Avilez & Kobayashi 1979). The precision of the present measurements does not uniquely establish one of the theoretical models, but is generally consistent in magnitude with expectations.

The difference between charmed-meson and -baryon production is clearly seen in Figure 33, which shows the $x_F$ distribution for the E 531 data. Half of the charmed baryons are target fragments while the charmed mesons are primarily identified as current fragments. It would appear that a reasonable fraction, perhaps one third, of the charmed-baryon production is quasi-elastic, and that charmed-baryon production is relatively small at high $Q^2$. It may thus be justifiably omitted at high $Q^2$ in the analysis of opposite-sign dimuon data to obtain the fraction of strange sea in the nucleon.
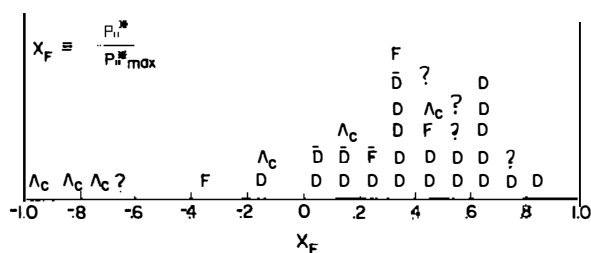


Figure 33  E 531 charm production characteristics. The figure shows the Feynman $x$ distribution for the E 531 charm events produced by neutrinos. $X_F$ is defined in terms of center-of-mass longitudinal momentum as shown in the figure. Note the target-like nature of three of the $\Lambda_c$ events with $X_F$ near $-1$.

The relative numbers of identified $D^0$, $D^+$, $D^{*+}$ are generally consistent, within present statistics, with the production ratios $D^*/D$ of about three, $D^+/D^0$ (not through $D^*$) of about one, and $D^{*+}/D^{*0}$ about the same. These are the expectations from the most naive assumption, i.e. relative population directly proportional to the number of spin states.

## 4.3   Opposite-Sign Dileptons

Because of the short lifetimes and relatively large semileptonic branching ratios of charmed particles, both counter and bubble chamber experiments have used the large numbers of easily identified, oppositely charged dilepton events to study the physics of deep inelastic charm production (see Figure 34 and Section 1.6). The helicity structure, assuming V–A currents, predicts the $y$ distribution to be flat, aside from the kinematic effect of transforming a light d or s quark to the heavy c quark. This threshold behavior changes the flat $y$ distribution to one peaked at higher $y$.

To create the high-mass quark $m_c$, the fraction of nucleon momentum $\xi$ carried by the interacting constituent becomes

$$\xi \approx x' = x + m_c^2/(2ME_\nu y), \qquad\qquad 28.$$

where $x$ is the traditional scaling variable ($Q^2/2M\nu$). This follows from the kinematics of the propagator four-momentum, $q$, combining with the quark whose momentum fraction is $x'p$ to give a mass $m_c^2$: $(q + x'p)^2 = -m_c^2$ (Barnett 1976, Georgi & Politzer 1976). The $x'$ variable then has a bound, $m_c^2/(2ME_\nu y)$, below which charm cannot be produced (Kaplan & Martin 1976).
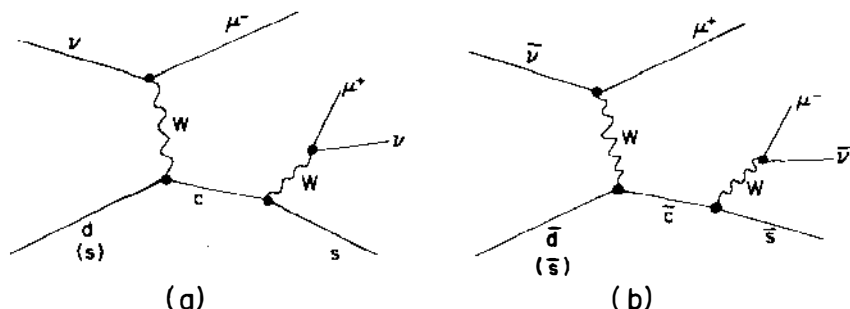


*Figure 34*   Feynman diagrams for production of dimuons through charm quark decay. Valence quarks (d) can only produce charm with neutrino beams. Hence the characteristics of dimuons from neutrino and antineutrino collisions are somewhat different.

For valence quarks, the charm cross section is not affected much in the low-$x'$ region, but for the strange-sea distribution, e.g. $x's(x') = A(1 - x')^7$, which is strongly peaked at small $x'$, there is substantial suppression at low neutrino (antineutrino) energies (Brock 1980, Edwards & Gottschalk 1981). If in addition to the assumption of $x'$ as the appropriate variable, one includes the phase space factor (slow rescaling) for producing a heavy quark in the two-body scattering, $\nu + [^d_s] \rightarrow \mu^- + c$, the charm production differential cross section becomes (Kaplan & Martin 1976, Lai 1978)

$$\frac{d^3\sigma}{dx\,dy\,dz} = \frac{G^2 M E_\nu}{\pi} \left\{ [x'd(x') \sin^2 \theta_c + x's(x') \cos^2 \theta_c] \right.$$
$$\left. \times \left[ 1 - \frac{m_c^2}{2 M E_\nu x'} \right] D(z) \right\}. \qquad 29.$$

In this equation the fragmentation of the charm quark is described by the function $D(z)$ where $z$ is the fraction of the energy taken by the charm particle (predominantly D mesons) in the W-boson-nucleon center of mass.

The rate for opposite-sign dileptons is then the cross section (Equation 29) multiplied by the average leptonic branching ratio for the decays of charmed particles. The D-meson leptonic branching ratios measured at SPEAR (Schindler et al 1981, Bacino et al 1980) imply an average charm to muon branching ratio of $0.08 \pm 0.03$, assuming a $D^0/D^+$ total production rate of 2 to 3. Since the E 531 data measure the relative charm to single muon cross section to be $7 \pm 2\%$ at 60 GeV, the expected $\mu^+\mu^-/\mu^-$ rate at comparable energy should be $\sim 0.55\%$ with the assumption of the branching ratio equal to 0.08. This is in good agreement with the dimuon rate at the same energy given in the next section and in Figure 35.

4.3.1 CHARM CROSS SECTION VS ENERGY   Several neutrino bubble chamber experiments have observed events with a muon and an electron in the final state ($\mu^- e^+$) (von Krogh et al 1976, Blietschau et al 1976, Deden et al 1977, Bosetti et al 1977a, 1978a, Baltay et al 1977, Erriquez et al 1978, Ballagh et al 1981). The phenomena have also been seen in antineutrino exposures ($\mu^+ c^-$) (Berge et al 1979, Ballagh et al 1977, 1981). These data come primarily from exposures to wide-band beams where the neutrino energy producing the event is not known *a priori*. The identification of positrons (electrons) is good with this technique for momenta above 0.3 GeV/$c$. However, only the energy
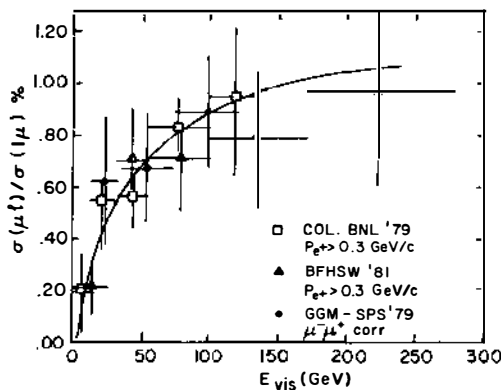
*Figure 35*  $\mu^- l^+ / \mu^-$ cross-section ratio vs $E_{vis}$. The data are $\mu^- e$ bubble chamber data from Ballagh et al (1981) and Murtagh (1979). The GGM-SPS data are $\mu^- \mu^+ / \mu^-$ rates corrected for full muon acceptance (Armenise et al 1979). $E_{vis}$ is the measured energy for the event, $E_{h^+} E_{\mu^-} + E_{l^+}$. The curve shown is a calculation that includes slow rescaling (Brock 1980).

visible to the apparatus $(E_{vis})$ is measured in an event; final-state neutrinos, for example, are lost. Thus, the $\mu^- e^+ / \mu^-$ relative cross sections for the experiments that report energy-dependent ratios are shown in Figure 35 as a function of $E_{vis}$. This shows that the dilepton cross section rises to 0.6% of the charged-current cross section at 50 GeV and then continues to rise to ~1% at 150 GeV.

There are several mechanisms in the production and decay of charmed mesons that should raise the number of neutral-strange-particle decays (V's) in events with charm. Much of the production involves transformation of an s quark, s→ c, leaving net strangeness behind. The subsequent decay of the charmed mesons decay preferentially to strange particles. Indeed, the number of observed strange particles per event is about four times as large in events with a prompt electron in the final states as in events without charm (Murtagh 1979). The raw numbers of excess neutral strange particles in $\mu e$ events seem to be generally agreed upon: ~0.3 per event. This is in reasonable agreement with the expectations of charm production (Murtagh 1979, Ballagh et al 1981).

Charm dimuon events are reported by both bubble chamber and counter experiments. However, for dimuons a substantial loss in signal results because the momentum of the second muon, $P_{\mu_2}$, is required to be larger than some minimum value. This cut is needed to eliminate confusion between hadrons and very low-momentum muons of short range as well as low-momentum muon background from the decays of $\pi$

and K mesons in the hadronic final state. The Gargamelle (Armenise et al 1979) and Fermilab E 546 (Ballagh et al 1980) collaborations have both measured dimuon rates with $P_{\mu_2} > 2.6$ and $4.0\,\mathrm{GeV}/c$, respectively. The $\mu^- \mu^+$ data of Gargamelle (117 events) corrected for the $P_{\mu_2}$ cut is shown in Figure 35 vs $E_{\mathrm{vis}}$ with the $\mu e$ bubble chamber data.

There are also recently published high-statistics cross-section rates for CDHS, CHARM, and CFRR. The CFRR data (484 $\nu$ events with $P_{\mu_2} > 4\,\mathrm{GeV}/c$) are obtained with the Fermilab dichromatic beam while the CDHS (15,000 events) and CHARM (494 $\nu$, 285 $\bar{\nu}$ events) data come from the CERN wide-band beam. A comparison of the CDHS and CFRR $2\mu/1\mu$ cross-section ratios for $P_{\mu_2} > 6.5\,\mathrm{GeV}/c$ shows reasonable agreement (Fisk 1981). To obtain the total dimuon rate, this restriction on muon momentum must be corrected with a theoretical model.

There is an additional problem associated with using wide-band beams for obtaining dimuon to single muon production ratios. The opposite-sign events from charm decay involve missing energy as discussed in the last section. For a typical case, e.g. $E_{\mathrm{missing}} \approx 15\,\mathrm{GeV}$ at 150-GeV incident energy, the dimuon events will be systematically underestimated in energy and compared to single muon events of lower energy, on average. Because wide-band beams provide flux with a substantial fall with energy, this can produce a systematic underestimate of the $2\mu/1\mu$ ratio by as much as 50%.

To find the total charm cross section, the CDHS group has employed a Monte Carlo calculation incorporating a specific charm model that corrects for the $P_{\mu_2}$ cut and includes the effects of the missing final-state $\nu$ energy. This allows them to establish the $2\mu/1\mu$ cross-section ratio as a function of $E_\nu$, rather than $E_{\mathrm{vis}}$ (Knobloch et al 1981). Their data have also had the K- and $\pi$-decay background of ~13% for $\nu$ and ~6% for $\bar{\nu}$ subtracted. The resulting cross-section points are shown in Figure 36. It should be pointed out that the CDHS antineutrino data derived from the wide-band beam have made a specific definition assigning the lower-energy muon to the charm decay. They have checked the reliability of this definition with a sample of narrow-band beam dimuons where the designation is not so arbitrary.

A comparison of the corrected CDHS neutrino and antineutrino data shows the $\bar{\nu}$ cross-section ratio to exceed the $\nu$ data at all energies. This is somewhat unexpected since slow rescaling should suppress the $\bar{\nu}$ rate more than the $\nu$ rate at low energies. This comes about because the $\bar{\nu}$ charm dimuons are produced entirely from sea quarks (see Equation 12). A calculation of the dimuon to single muon rate depends sensitively (see Section 1.6) on the valence and sea $x$ distribution, the charm quark
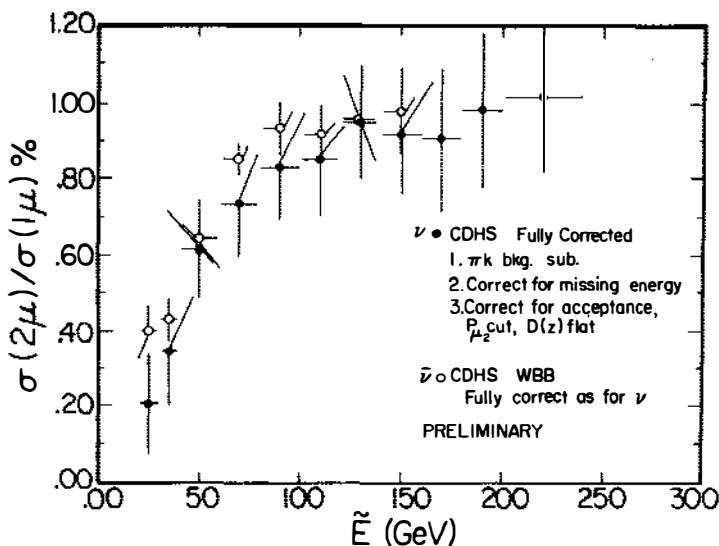
**Figure 36** CDHS corrected opposite-sign dimuon rates for neutrinos and antineutrinos. The data, accumulated during wide-band beam operation, have been corrected using a Monte Carlo program for (*a*) the $P_{\mu_2}$ cut, (*b*) missing final-state energy, and (*c*) background due to hadronic decays to muons (Knobloch et al 1981). $\tilde{E}$ is the Monte-Carlo-corrected energy, which includes an estimate of the missing final-state neutrino energy.

mass, and the fraction of strange sea in the nucleon (Edwards & Gottschalk 1981).

4.3.2 *x* DISTRIBUTIONS    Figure 37 shows the *x* distributions of dimuon events obtained by CDHS in their wide-band running without corrections for apparatus acceptance, which they have calculated to be negligible (Knobloch et al 1980). Both neutrino and antineutrino data are shown. The quantity histogrammed is $x_{vis}$, which is usually about 10% larger than the true *x* owing to missing neutrino energy. The mean values of $x_{vis}$ for the neutrino and antineutrino data shown are $0.195 \pm 0.01$ and $0.095 \pm 0.01$, respectively. Both CFRR (Fisk 1981) and CHARM (Jonker et al 1981a) experiments are in qualitative agreement with these *x* distributions. The striking difference between the $\nu$ and $\bar{\nu}$ *x* distributions clearly indicates the production of charm for antineutrinos almost exclusively from the charm-sea quarks while the neutrino data show production from both sea and valence quarks.

4.3.3    STRANGE-SEA CONTENT OF THE NUCLEON    Two methods have been used to extract the strange-sea content of the nucleon:
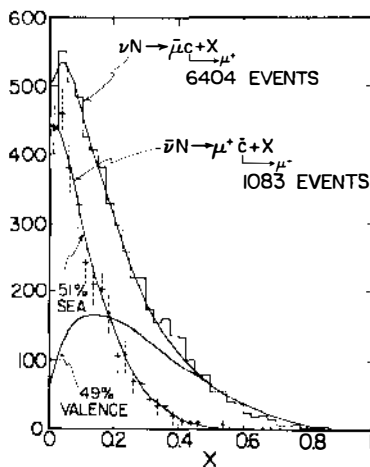
*Figure 37* CHDS $x$ distributions for opposite-sign dimuons. The $x_{vis}$ distributions for CDHS wide-band neutrino and antineutrino dimuon data are shown. As expected the antineutrino data are sharply peaked at small $x$ since charm production occurs almost entirely by conversion of an anti-strange-sea quark to an anti-charm quark. The neutrino charm production involves both the valence down quarks and sea strange quarks. The valence distribution alone is also shown (Buras & Gaemers 1978). The neutrino data are fitted with 51% strange sea and 49% valence quarks. $x_{vis}$ is the $x$ value calculated using the visible energy for $E_\nu$.

$\eta_s = 2S/(U + D)$, where $S$, $U$, and $D$ refer to the integrals over $x$ of the appropriate momentum fractions, e.g. $U = \int xu(x) \, dx$. In the first method the neutrino dimuon $x$ distribution is fitted using the valence $x$ distributions, $u(x)$ and $d(x)$, obtained from deep inelastic scattering and the strange sea, $s(x)$ from the opposite-sign antineutrino dimuons. For example, CDHS assume a Buras-Gaemers (Buras & Gaemers 1978) valence distribution and $A(1 - x)^7$ for the strange sea, both features being qualitatively consistent with their data in shape, to obtain $\eta_s$.

The second or double ratio method is based not on $x$ distributions but on the ratios

$$R_1 = \frac{\sigma_{\bar{\nu}}(1\mu)}{\sigma_\nu(1\mu)}$$

$$R_2 = \frac{\sigma_\nu(2\mu)/\sigma_\nu(1\mu)}{\sigma_{\bar{\nu}}(2\mu)/\sigma_{\bar{\nu}}(1\mu)}$$

to find $\eta_s$. Assuming $\eta \equiv \bar{U} + \bar{D}/U + D \approx 0.15$, the fraction of strange sea is given by

$$\eta_s = \frac{\tan^2 \theta_c[1 - \eta R_2/R_1]}{[R_2/R_1 - 1]}.$$

CDHS and CHARM have reported values of $\eta_s$. Figure 38 shows the CDHS results, determined using the two methods, as a function of $E_\nu$ (Knobloch et al 1981). The overall average value of $\eta_s$ is $0.046 \pm 0.006$, not including slow rescaling or systematic errors. Similarly the CHARM group finds $\eta_s = 0.050 \pm 0.015$ again without slow rescaling (Jonker et al
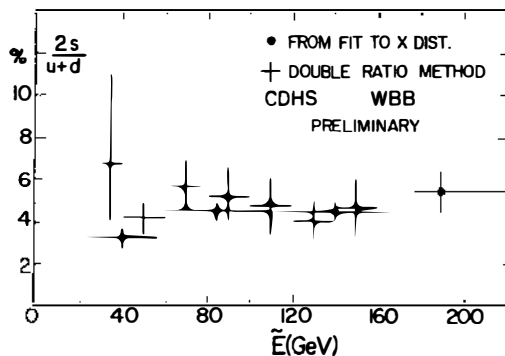
*Figure 38*  CDHS determination of the strange-sea fractional momentum in the nucleon
(Knobloch et al 1981). Two methods are used to determine the strange-sea fraction,
$\eta_s \equiv 2S/(U+D)$. The first technique (*solid points*) uses the neutrino $x$ distribution as fitted
in Figure 37 to obtain $\eta_s$, while the second method, discussed in Section 4.3, employs the
double ratio technique. Slow rescaling effects have not been taken into account.
Preliminarly indications suggest they would approximately double $\eta_s$ (Knobloch et al
1981).

1981a). The effects of slow rescaling could double the value of $\eta_s$
(Knobloch et al 1981, Edwards & Gottschalk 1981), making it ~10%,
which is still less than is expected for an SU(3) symmetric strange sea,
i.e. $\eta_s = \eta = 12-15\%$. It should be emphasized that quantitative results
on the magnitude of the strange sea have only become available recently
and the effects of slow rescaling have not been reported by the groups
who have sizable data samples.

4.3.4  CHARM FRAGMENTATION    Since the dimuon experiments do not
measure the energy of the charmed particle, the charm fragmentation
function is difficult to determine. Based on models of charm production
that include the assumption of production of only D or D* mesons, one
can fit the $z_{\mu 2}$ distribution, i.e. the fraction of energy carried off by the
charm-produced second muon, to determine the fragmentation func-
tion. Generally the experiments seem to agree that the $z$ distribution is
flat or peaked toward larger $z$, although most of the data on this subject
is still preliminary. The hybrid emulsion experiment should give some
insight into this problem albeit with small statistics and at lower
energies.

4.3.5  SUMMARY    In summary, the qualitative features of charm pro-
duction by neutrinos (antineutrinos) appears to agree with the basic
GIM model, which predicts that the charm production should rise to a

value determined by the valence d and sea-strange quarks. The $x$ distributions indicate the important role taken by the strange-sea quarks, and the energy dependence of the charm cross section exhibits threshold dependence that may be accounted for by slow rescaling. The momentum fraction of strange sea in the nucleon is 4–5% and could be double that with slow rescaling. This is an important point especially because knowledge of the magnitude of the strange sea is essential in comparing deep inelastic muon and neutrino scattering (see Section 3.3.3).

## 4.4    *Like-Sign Dimuons*

Several experimental groups have reported the observation of like-sign dimuons, although the level of the signals and backgrounds have not always agreed. All experiments conclude that the second muon originates at the hadron vertex. This follows from the fact that the $\phi$ distribution is peaked at 180°, where $\phi$ is the angle between the two muon tracks projected on a plane perpendicular to the incident neutrino (de Groot et al 1979a, Nishikawa et al 1981, Benvenuti et al 1978a). Mechanisms suggested as prompt sources for these signals include (*a*) associated charm production, (*b*) bottom meson or baryon production, and (*c*) $D^0 - \bar{D}^0$ mixing.

4.4.1    ENERGY DEPENDENCE OF THE LIKE-SIGN RATE    A summary of recent experimental $\mu^-\mu^-/\mu^-$ rates is shown in Figure 39 (Knobloch et al 1981, Jonker et al 1981a, Holder et al 1977, Trinko et al 1981, Shaevitz et al 1980). To substantially reduce the background from second muons coming from the decay of K and $\pi$ mesons, a $P_{\mu_2} > 9$-GeV cut has been imposed on most of the data. Note that the results come from experiments that use narrow-band, horn, and quadrupole triplet beams. As mentioned earlier, in the discussion of opposite-sign dimuon rates, for data taken in horn beams this can lead to an underestimate of the cross-section ratio that cannot be compensated by calculation, in this case, since the mechanism producing the like-sign dimuon is unknown. Narrow-band beam data do not suffer from this problem but are typically less statistically significant.

4.4.2    BACKGROUND CALCULATIONS    Although the $P_{\mu_2}$ cut eliminates most of the background, calculations must still be made to determine an absolute background level. Such a calculation, which is based directly on experimental data, is discussed by Shaevitz et al (1980). The anticipated background sources are: (*a*) decay of primary $\pi$'s or K's produced at the hadron vertex in ordinary single-muon charged-current
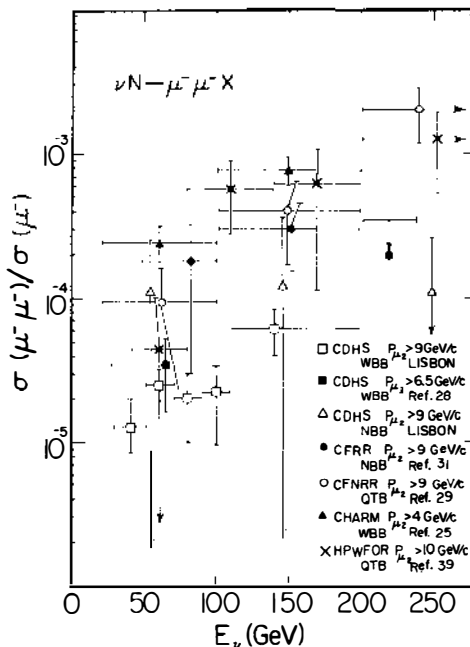
*Figure 39* Like-sign dimuon rates. The rates for $\nu N \rightarrow \mu^-\mu^- X$ relative to the single muon charged-current cross section are shown. The data include the momentum cut for the second muon as shown. References from the top to the bottom of the list are Knobloch et al 1981, Holder et al 1977, de Groot et al 1979, Shaevitz et al 1980, Nishikawa et al 1981, Jonker et al 1981, and Trinko et al 1981. The CDHS open triangles and the CFRR data are taken with the narrow-band beam. The CFNRR and HPWFOR data were obtained with the quadrupole triplet beam and the remaining CDHS and CHARM data result from wide-band beam experiments. The one-standard-deviation upper limit shown at 220 GeV is from the CFRR experiment.

interactions, and (*b*) the production of either a prompt or nonprompt second muon from the interaction of the primary hadrons in the hadron shower. The rate from decays of the primary hadrons is calculated two ways. The $\pi$ and K inclusive spectra and multiplicity are determined either from Field-Feynman quarks jets based on $\nu$Ne data obtained with a wide-band beam or they are taken directly from high-energy $\nu$Ne data. The secondary particle cascade calculation makes use of the hadrons just described and the measured prompt and nonprompt muon production by hadrons in the Fermilab experiment E 379/595 variable density target. This yields the probability, as a function of hadron energy $E_H$, for producing a muon with momentum greater than a particular cutoff value. An example of the calculation is given in Figure 40.

The calculated numbers of background events is obtained from the convolution of the probability curve with the observed hadron energy distribution for single-muon events. In the first experiment (CFNRR) definitively to see a signal, there were 12 events with $1.3 \pm 0.7$ background (Nishikawa et al 1981). In the more recent CFRR narrow-band data there are $13 \, \mu^- \mu^-$ events and the calculated background is 3.5 events. Calculations that roughly agree with this background rate have been made by CDHS and HPWFOR (de Groot et al 1979a, Trinko et al 1981). The HPWFOR and CFNRR groups have checked their background calculation by comparing it with the $\mu^- \mu^+ / \mu^-$ rates they obtain in different target densities.

The CHARM collaboration group with $P_{\mu_2} > 4 \, \mathrm{GeV}/c$ did not make a background subtraction but instead extrapolated both muons back to the event vertex, where they can find the projected horizontal and vertical distances between the two muons. A comparison of this distribution with those for prompt and decay muons generated by
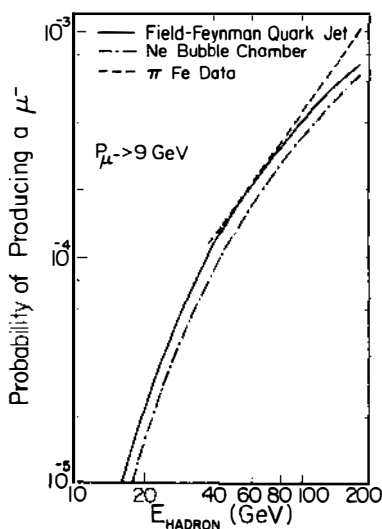


*Figure 40* Muon production probability vs hadron energy. The curves are the probability vs hadron energy that a $\mu^-$ with momentum greater than 9 GeV/c will be produced and observed in the CFRR detector from $\pi$ or K decay. The solid curve uses the Field-Feynman quark jets to generate the hadrons. The dashed curve, given for comparison to the solid curve, is the measured probability with pions on the CFRR detector (Shaevitz et al 1980). The dot-dashed curve utilizes neon bubble chamber data on hadronic final states from neutrino collisions to calculate the first-generation decays and the $\pi$Fe data for subsequent generations.

Monte Carlo techniques gives them the fraction of prompt events in their sample.

Although the data shown in Figure 39 do not all agree, there is good agreement among the narrow-band and quadrupole triplet data. The above discussion does leave some room for differences in normalization and background subtractions. In any case, a level of $10^{-4}$ at 200 GeV is difficult to obtain with present theoretical models.

4.4.3    POSSIBLE SOURCES OF LIKE-SIGN DIMUONS    The earliest predictions of like-sign dimuons resulted from considering the associated production of charmed pairs, $c\bar{c}$ as shown in Figure 41$a$ (Goldberg 1977, Young et al 1978, Kane et al 1979). These authors concluded that for the same cuts on the theory as experiment, the predicted like-sign rate is low compared to the data by one to two orders of magnitude. As an aside comment it should be pointed out that theoretical predictions for



(a)
**Gluon Bremsstrahlung**



(b)
**Intrinsic Charm**
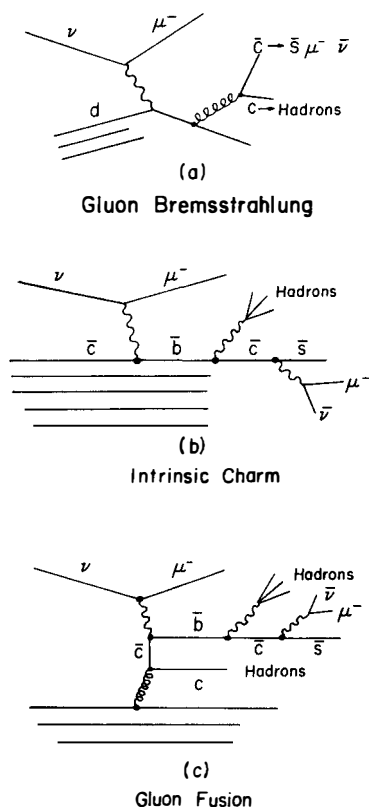
*Figure 41*  Possible sources for like-sign dimuons. (*a*) Associated charm production by gluon bremsstrahlung (Goldberg 1977, Young et al 1978, Kane et al 1979). (*b*) b production with intrinsic charm (Brodsky et al 1981). (*c*) b production via gluon fusion (Barger et al 1981).



(c)
**Gluon Fusion**

hadronic production of bare charm pairs by gluon bremsstrahlung are also lower than the observed rate by one or two orders of magnitude.

As an example of b (bottom quark) production, Brodsky, Peterson & Sakai (Brodsky et al 1981) proposed intrinsic charm within the nucleon (Figure 41b) to explain neutrino like-sign dimuon rates and the large diffractive cross section claimed for pp → $\Lambda_c^+$ at the ISR (Giboni et al 1979). With 1% intrinsic charm and $p_{\mu_2} > 9$ GeV/$c$, the model gives too small a rate. The rate is severely limited partly because of the V − A coupling of c to b quarks, which gives a $(1 - y)^2$ factor in the cross section. They point out that intrinsic charm would give a like-sign dimuon $x$ distribution whose mean value is significantly larger than is the case for gluon bremsstrahlung.

Barger, Keung & Phillips (Barger et al 1981) investigated a b-production model with gluon fusion, as shown in Figure 41c. They find the cross section for this process to be smaller than the intrinsic charm model and conclude that of the three models discussed, the intrinsic charm model with full strength right-handed coupling comes closest to fitting the data. If the rate is to be explained with left-handed (V − A) coupling, the intrinsic charm in the nucleon would have to be more than 1% and this is inconsistent with the large-$x$ dimuon cross section observed in muon scattering by the EMC group (Strovink 1981).

If there were sufficient $D^0 - \bar{D}^0$ mixing, then same-sign dimuons would follow from the same mechanisms producing opposite-sign events. For example, if all the like-sign dimuons in the CFRR experiment came from $D^0 - \bar{D}^0$ mixing, the $D^0/D^+$ production ratio plus $D^0 \rightarrow \mu$ inclusive branching ratio would imply $D^0 - \bar{D}^0$ mixing at about 20%. At the present time, there is no evidence for mixing with the measured limits (90% confidence level) of less than 11% (Avery et al 1980) and (95% confidence level) of less than 16% (Feldman et al 1977). And there is evidence from hadronic interactions that the mixing limit is even smaller than this (Bodek et al 1982). This strongly suggests that the fraction of like-sign events due to mixing is negligible.

Thus, we conclude that several experiments see evidence for like-sign dimuons, but there is at present no single source to account for them.

## 5.  SUMMARY

The study of charged-current neutrino interactions with nucleons has confirmed our understanding of the V − A nature of the charged weak current. It has also provided, through the measurement of nucleon structure functions, corroboration of the quark model. The predominantly spin-$\frac{1}{2}$ nature of the quarks is shown in the charged-current

neutrino and antineutrino $y$ distributions. The approximate correctness of scaling is demonstrated by the linear rise of the neutrino cross section with energy. Measurements of neutrino and antineutrino cross sections give integrated values of the structure function $F_2(x)$ implying that only half of the nucleon's longitudinal momentum is carried by the quarks. The remaining momentum is presumably taken by the gluons that carry the strong forces between quarks. Comparison of the structure function $F_2$, as measured separately with muons and neutrinos, convincingly demonstrates the existence of fractional charge for the quark partons. That the number of valence quarks in the nucleon is three has also been approximately verified with the measurement of the integral of $F_3(x)$ (Gross-Llewellyn Smith sum rule). Any disagreement in these fundamental tests ($<20\%$) is probably within present experimental precision among all the various experiments.

The flavor-changing nature of the weak hadronic current permits the observation of neutrino-induced opposite-sign dimuon events. Here the second muon results from the semileptonic decay of a charmed hadron. In particular, the antineutrino dimuon data, that come primarily from the conversion of an $\bar{s}$ to a $\bar{c}$ quark, allow measurement of the strange sea quark $x$ distribution. Experimentally the neutrino-induced charm states, as observed in emulsion, have provided lifetimes for the $D^{+-}$, $D^0$, $F^{+-}$, and $\Lambda_c$ states, and as more data become available will give information on charm fragmentation. The origin of like-sign dimuons observed at a rate about 10% of the opposite-sign dimuons is not well understood but may be due to associated charm production.

Deviations from the simple quark model and scaling hypothesis occur in the structure functions at fixed $x$ as $Q^2$ is varied. The theory of perturbative quantum chromodynamics (QCD) predicts such nonscaling behavior. How much of the observed $Q^2$ variation is related to perturbative QCD remains to be determined. If the $Q^2$ dependence is dominated by perturbative QCD diagrams, the dependence of the structure functions should be approximately logarithmic with $Q^2$. The amount of variation permits a measurement of the quark-gluon coupling constant, $\alpha_s$, or alternatively the scale parameter of the strong interactions, $\Lambda$. Values of $\Lambda$ from muon and neutrino structure function measurements are presently in the vicinity of 100 to 250 $(\text{MeV}/c)^2$. An alternative determination of $\alpha_s$ may result from the measurement of the $R$ parameter ($\sigma_L/\sigma_T$). Present data that reach a maximum $Q^2$ of about 200 $(\text{GeV}/c)^2$, along with new data at larger $Q^2$ which will be available at Tevatron energies, should provide more conclusive tests of QCD. This presumes, of course, that there are no new surprises to be uncovered in charged-current phenomena in that energy region.

## Literature Cited

Abramowicz, H., et al. 1981. *Phys. Lett.* 107B:141–44

Abramowicz, H., et al. 1981a. *Nucl. Instrum. Methods* 180:429

Adler, S. L. 1966. *Phys. Rev.* 143:1144

Allasia, D., et al. 1979. *Phys. Lett.* 87B:287

Altarelli, G. Martinclli, G. 1978. *Phys. Lett.* 76B:89

Altarelli, G., et al. 1974. *Phys. Lett.* 48B:435

Altarelli, G., Parisi, G. 1977. *Nucl. Phys.* B126:298

Amer, A., et al. 1979. *Phys. Lett.* 81B:48

Ammar, R., et al. 1980. *Phys. Lett.* 94B:118

Angelini, C., et al. 1979a. *Phys. Lett.* 80B:428

Angelini, C., et al. 1979b. *Phys. Lett.* 84B:150

Appelquist, T., Barnett, R. M., Lane, K. 1978. *Ann. Rev. Nucl. Part. Sci.* 28:387–499

Armenise, N., et al. 1979. *Phys. Lett.* 86B:115

Armenise N., et al. 1981. *Phys. Lett.* 104B:409

Astratyan, A. E., et al. 1978. *Phys. Lett.* 105B:315

Atherton, H. W., et al. 1980. *CERN Preprint 80–07* (unpublished)

Aubert, J. J., et al. 1981. *Phys. Lett.* 105B:315

Aubert, J. J., et al. 1981a. *Phys. Lett.* 105B:322

Avery, P., et al. 1980. *Phys. Rev. Lett.* 44:1309

Avilez, C., Kobayashi, T. 1979. *Phys. Rev.* D19:3448

Avilez, C., et al. 1978. *Phys. Rev.* D17:709

Bacino, W., et al. 1980. *Phys. Rev. Lett.* 45:329

Ballagh, H. C., et al. 1977. *Phys. Rev. Lett.* 39:1650

Ballagh, H. C., et al. 1980. *Phys. Rev.* D21:569

Ballagh, H. C., et al. 1981. *Phys. Rev.* D24:7

Baltay, C. 1981. *Proc. Neutrino '81*, ed. R. J. Cence, E. Ma, A. Roberts, 2:195–328. (Maui, Hawaii)

Baltay, C., et al. 1977. *Phys. Rev. Lett.* 39:62

Baltay, C., et al. 1978, *Phys. Rev. Lett.* 41:73

Baltay, C., et al. 1979. *Phys. Rev. Lett.* 42:1721

Bardeen, W. A., et al. 1978. *Phys. Rev.* D18:3998

Barger, V., et al. 1981. *Phys. Rev.* D24:244

Barish, B. C., et al. 1975. *Nucl. Instrum. Methods* 130:49

Barish, B. C., et al. 1977. *Phys. Rev. Lett.* 39:1595

Barish, B. C., et al. 1978. *Phys. Rev. Lett.* 40:1414

Barish, B. C., et al. 1978a. *IEEE Trans. Nucl. Sci.* NS-25:532

Barish, S. J., et al. 1979. *Phys. Rev.* D19:2521

Barnett, R. M. 1976. *Phys. Rev. Lett.* 36:1163

Benvenuti, A., et al. 1977. *Phys. Rev. Lett.* 38:1110

Benvenuti, A., et al. 1978. *Phys. Rev. Lett.* 40:488

Benvenuti, A., et al. 1978a. *Phys. Rev. Lett.* 41:725

Berge, J. P., et al. 1979. *Phys. Lett.* 81B:89

Beuselinck, R., et al. 1978. *Nucl. Instrum. Methods* 154:445

Bjorken, J. D., Paschos, E. A., 1969. *Phys. Rev.* 185:1975

Blair, R. E. 1982. PhD thesis. *A Total Cross Section and y-Distribution Measurement for Muon-Type Neutrinos and Anti-Neutrinos on Iron*, Caltech, Pasadena

Blietschau, J., et al. 1976. *Phys. Lett.* 60B:207

Blietschau, J., et al. 1979. *Phys. Lett.* 86B:108

Bodek, A., et al. 1973. *Phys. Rev. Lett.* 30:1087

Bodek, A., et al. 1979. *Phys. Rev.* D20:1471

Bodek, A., Ritchie, J. L. 1981. *Phys. Rev.* D23:1070; D24:1400

Bodek, A., et al. 1982. *Phys. Lett.* 113B:82

Bofill, J., et al. 1982. *IEEE Trans Nucl. Sci.* NS-29 1:400

Bogert, D., et al. 1982. *IEEE Trans. on Nucl. Sci.* NS-29 1:363

Bollini, D., et al. 1981. *Phys. Lett.* 104B:403

Bosetti, P.C., et al. 1977. *Phys. Lett.* 70B:273

Bosetti, P. C., et al. 1977a. *Phys. Rev. Lett.* 38:1248

Bosetti, P. C., et al. 1978. *Nucl. Phys.* B142:1–28

Bosetti, P. C., et al. 1978a. *Phys. Lett.* 73B:380

Bosio, C., et al. 1978. *Nucl. Instrum. Methods* 157:35

Brand, C., et al. 1978. *Nucl. Instrum. Methods* 136:485

Brand, C., et al. 1982. *IEEE Trans. Nucl. Sci.* NS-29 1:272

Brock, R. 1980. *Phys. Rev. Lett.* 44:1027
Brodsky, S. J., et al. 1981. *Phys. Rev.* D23:2745
Buras, A. J., Gaemers, K. J. F. 1978. *Nucl. Phys.* B132:249
Burhop, E. H. S., et al. 1976. *Phys. Lett.* 65B:299
Büsser, F. W. 1981. See Baltay 1981, p. 351
Cabibbo, N. 1963. *Phys. Rev. Lett.* 10:531
Callan, C. G., Gross, D. J. 1969. *Phys. Rev. Lett.* 22:156
Cazzoli, E. G., et al. 1975. *Phys. Rev. Lett.* 34:1125
Cence, R. J., et al. 1976. *Nucl. Instrum. Methods* 138:245
Chapman-Hatchett, A., et al. 1979. *CERN Rep. SPS/ABT/Int. 79-1* (unpublished)
Close, F. E. 1979. *An Introduction to Quarks and Partons.* New York: Academic
Cnops, A. M., et al. 1979. *Phys. Rev. Lett.* 42:197
Danby, G., et al. 1962. *Phys. Rev. Lett.* 9:36
Deden, H., et al. 1977. *Phys. Lett.* 67B:474
de Groot, J. G. H., et al. 1979. *Z. Phys.* C1:143
de Groot, J. G. H., et al. 1979a. *Phys. Lett.* 86B:103
de Groot, J. G. H., et al. 1980. *Proc. 20th Int. Conf. High Energy Phys.*
Diddens, A. N., et al. 1980. *Nucl. Instrum. Methods* 178:27
Dishaw, J. P., et al. 1979. *Phys. Lett.* 85B:142
Edwards, B. J., Gottschalk, T. D. 1981. *Nucl Phys.* B186:309
Edwards, D. A., Sciulli, F. J. 1976. *A Second Generation Narrow Band Neutrino Beam. FERMILAB TM-660* (unpublished)
Eichten, T., et al. 1973. *Phys Lett.* 46B:274
Eisele, F., et al. 1981. See Baltay 1981, 1:297–310; also, private communication with R. Turlay
Erriquez, O., et al. 1978. *Phys. Lett.* 77B:227
Farrar, G. 1974. *Nucl Phys.* B77:429–42
Feldman, G. J., et al 1977. *Phys. Rev. Lett.* 38:1313
Feynman, R. P. 1969. *Phys. Rev. Lett.* 23:1415
Feynman, R. P. 1972. *Photon-Hadron Interactions.* Reading, Mass: Benjamin
Feynman, R. P. 1974. *Proc. Neutrino '74,* ed. C. Baltay, pp. 299–327. New York: Am. Inst. Phys.
Finjord, J., Ravndal, F. 1975. *Phys. Lett.* 58B:61
Fisk, H. E. 1981. *Proc. Int. Symp. Leptons*

*Photons High Energies,* ed. W. Pfeil, p. 703. Univ. Bonn Phys. Inst.
Fritze, P., et al. 1981. See Baltay 1981, 1:344–48
Gaillard, M. K. 1974. See Feynman 1974, p. 65
Gaillard, M. K., et al. 1975. *Rev. Mod. Phys.* 47:277
Gell-Mann, M. 1964. *Phys. Lett.* 8:214
Gell-Mann, M., Levy, M. 1960. *Nuovo Cimento* 16:705
Georgi, H. Politzer, H.D.. 1976. *Phys. Rev.* D14:1829
Giboni, K. L., et al. 1979. *Phys. Lett.* 85B:437
Giesch, M., et al. 1963. *Nucl. Instrum. Methods* 20:58
Glashow, S., ct al. 1970. *Phys. Rev.* D2:1285
Goldberg, H. 1977. *Phys. Rev. Lett.* 39:1598
Gonzalez-Arroyo, H. L., et al. 1979. *Nucl. Phys.* B153:161; B159:512
Gonzalez-Arroyo, H. L., et al. 1980. *Nucl. Phys.* B166:429
Gordon, B. A., et al. 1979. *Phys. Rev.* D20:2645–91
Grassler, H., et al. 1981. *Phys. Lett.* 99B:159
Grimson, J., Mori, S. 1978. New Single Horn System. *FERMILAB TM-824* (unpublished)
Gross, D. J., Llewellyn Smith, C. H. 1969. *Nucl. Phys.* B14:337
Gunion, J. F. 1974. *Phys. Rev.* D10:242–50
Heagy, S. M., et al. 1981. *Phys. Rev.* D23:1045–69
Holder, M., et al. 1977. *Phys. Rev. Lett.* 39:433
Holder, M., et al. 1978. *Nucl. Instrum. Methods* 148:235; 151:69
Hung, P. Q., Sakurai, J. J. 1981. *Ann. Rev. Nucl. Part. Sci.* 31:375–438
Jonker, M., et al. 1981. *Phys Lett.* 99B:265; Erratum 100B:520
Jonker, M., et al. 1981a. *Phys. Lett.* 107B:241
Kane, G. L., et al. 1979. *Phys. Rev.* D19:1978
Kaplan, J., Martin, F. 1976. *Nucl. Phys.* B115:333
Kitagaki, T., et al. 1980. *Phys. Rev. Lett.* 45:955
Kitagaki, T., et al. 1982. *Phys. Rev. Lett.* 48:299
Knobloch, J., et al. 1980. *Proc. 20th Int. Conf. High Energy Phys. Madison, Wis.,* ed. L. Durand, L. Pondrom, p. 769. New York: Am. Inst. Phys.
Knobloch, J., et al. 1981. See Baltay 1981, 1:421
Lai, C. H. 1978. *Phys. Rev.* D18:1422

Lee, J. R. 1980. PhD thesis. *Measurements of νN Charged Current Cross Sections from 25 to 260 GeV*, Caltech, Pasadena (Unpublished)

Limon, P., et al. 1974. *Nucl. Instrum. Methods* 116:317

Lubimov, V. A., et al. 1980. *Phys. Lett.* 94B:266

Mann, A. W., et al. 1973. *Phys. Rev. Lett.* 31:844

Marel, G., et al. 1977. *Nucl. Instrum. Methods* 141:43

May, J., et al. 1977. Status Report on Narrow Band Neutrino Beam Running and Monitoring, *CERN Internal Rep. 26.4.7* (unpublished)

Mestayer, M. D. 1978. PhD thesis. *SLAC Rep. No. 214* (unpublished)

Miller, G. et al. 1972. *Phys. Rev. D5*:6528

Morfin, J., et al. 1981. *Phys. Lett.* 104B:235

Mount, R. P. 1981. *Nucl. Instrum. Methods* 187:401

Murtagh, M. J. 1979. *Proc. 1979 Int. Symp. Lepton Photon Interact. High Energies*, ed. T. B. W. Kirk, H. D. I. Arbarbane p. 277. Batavia, Ill: Fermi: Natl. Lab

Nachtmann, O. 1973. *Nucl. Phys. B63*:237

Nishikawa, K., et al. 1981. *Phys. Rev. Lett.* 46:1555

Perkins, D. H. 1978. *Proc. Summer Inst. Part. Phys.* p. 1. Stanford, Calif: SLAC

Peterson, V. Z. 1964. A Monochromatic Neutrino Beam from a High Intensity 200-GeV Proton Synchrontron. *LRL Rep. UCID-10028* (unpublished)

Pontecorvo, B. 1951. *J. Exp. Theor. Phys. (USSR)* 37:1751 (Transl. 1960. *Sov. Phys. JETP* 10:1236)

Pontecorvo, B. 1957. *Sov. Phys. JETP* 6:429, 1972

Primakoff, H., Rosen, S. P. 1981. *Ann. Rev. Nucl. Part. Sci.* 31:145–92

Rapidis, P., et al, 1981. *Proc. Summer Inst. Part. Phys.*, ed. A. Mosher, p. 641. Stanford, Calif: SLAC

Reya, E. 1981. *Phys. Rep.* 69:195–333

Rubbia, C., et al. 1974. *Proc. 17th Int. Conf. High Energy Phys., London*, ed. J. R. Smith, p. IV-117. Chilton: Sci. Res. Counc. Rutherford Lab.

Sakurai, J. J. 1981. See Baltay 1981, 2:457–91

Schindler, R. H., et al. 1981. *Phys. Rev.* 24:78

Schmidt, I. A., Blankenbecler, R. 1977. *Phys. Rev. D16*:1318

Schrock, R. E., Lee, B. W. 1976. *Phys. Rev. D13*:2539

Schwartz, M. 1960. *Phys. Rev. Lett.* 4:306

Sciulli, F. 1980. *Proc. Summer Inst. Part. Phys.* ed. A. Mosher, p. 29. Stanford, Calif: SLAC

Sciulli, F., et al. 1970. Neutrino Physics at Very High Energies, *Fermilab Proposal 21* (unpublished)

Shaevitz, M. H., et al. 1980. See Sciulli 1980, p. 475

Shaevitz, M., et al. 1981. See Balty 1981, 1:311

Shultze, K. 1977. *Proc. 1977 Int. Symp. Lepton Photon Interact. High Energy, Hamburg, Germany*, p. 359. Hamburg: DESY

Skuja, A., et al. 1976. The 300-GeV Triplet Train. *Fermilab TM-646* (unpublished)

Smadja, G. 1981. See Fisk 1981, p. 444

Söding, P., Wolf, G. 1981. *Ann. Rev. Nucl. Part. Sci.* 31:231–93

Stanton, N. R. 1981. See Baltay 1981, 1:491

Stefanski, R., White, H. 1976. Neutrino Flux Distributions. *Fermilab FN-292* (unpublished)

Stevenson, M. L. 1978. *Proc. Topical Conf. Neutrino Phys. Accel., Oxford*, ed. A. G. Michette, P. B. Renton, p. 362. Chilton, England: Rutherford Lab.

Strovink, M. 1981. See Fisk 1981, p. 594

Stutte, L., et al. 1981. See Baltay 1981, 1:377

Taylor, F. E., et al. 1978. *IEEE Trans. Nucl. Sci.* NS-25:31

Taylor, F. E., et al. 1980. *IEEE Trans. Nucl. Sci.* NS-27:30

Trilling, G. H. 1980. See Knobloch et al 1980, p. 1140

Trinko, T., et al. 1981. *Phys.. Rev. D23*:1889

Ushida, N., et al. 1980a. *Phys. Rev. Lett.* 45:1049

Ushida, N., et al. 1980b. *Phys. Rev. Lett.* 45:1053

Ushida, N., et al. 1982. *Phys. Rev. Let.* 48:844

van der Meer, S., et al. 1963. *Proc. Siena Int. Conf. Elementary Part.* 1:536, ed. G. Bernardin:, G. P. Puppi. Bologna: Soc. Ital. Fis.

von Krogh, J., et al. 1976. *Phys. Rev. Lett.* 36:710

Wachsmuth, H. 1977. *CERN Rep. EP/PHYS 77-43* (unpublished)

Willis, S. E., et al. 1980. *Phys. Rev. Lett.* 45:1370

Young, B. L., et al. 1978. *Phys. Lett.* 74B:111

Zweig, G. 1964. *CERN Reps. 8182/TH 401; 8419/TH 412* (unpublished)